



UNIVERSITÀ
DEGLI STUDI
DI PADOVA

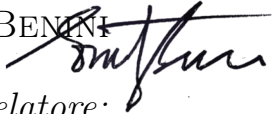
UNIVERSITÀ DEGLI STUDI DI PADOVA

DIPARTIMENTO DI INGEGNERIA INDUSTRIALE DII
CORSO DI LAUREA IN INGEGNERIA MECCANICA

TESI DI LAUREA MAGISTRALE

A Body Force Method Implementation in a Computational Fluid Dynamics Solver

Laureando:
Alessandro PICCOLI

Relatore:
Prof. Ernesto BENINI

Correlatore:
Ing. Andrea MAGRINI

Anno accademico 2019 / 2020

Sommario

I futuri aerei di linea pongono nuove sfide in ambito progettuale, specialmente per quanto concerne la progettazione dei motori. Nell'ottica di ridurre i consumi e le emissioni rumorose, i motori saranno racchiusi in gondole dal diametro sempre maggiore per aumentarne il rapporto di by-pass. Di contro, per compensare i maggiori ingombri, le gondole presenteranno tratti iniziali più accorciati e dunque interazioni aerodinamiche più accentuate tra la presa d'aria e il fan. Per acquisire e caratterizzare queste interazioni diventano necessarie, in fase di progetto, tecniche numeriche veloci ed accurate. A tal riguardo in questa tesi viene presentata una particolare classe di metodi, noti con l'appellativo di "Body Force Methods", in cui le schiere palari di una turbomacchina vengono sostituite da termini sorgente che riproducono la deviazione fluida e le perdite. Uno specifico metodo body force, basato sull'analogia di lift e drag, viene spiegato nel dettaglio e quindi implementato in un solutore di fluidodinamica computazionale. Il metodo è costituito da tre sotto modelli: un modello di forza normale (rispetto alla direzione di deflusso), un modello di forza parallela viscosa e un modello per il bloccaggio metallico delle pale. Ciascuno dei precedenti ricostruisce diversi aspetti dell'interazione fluido-schiera: la forza normale modifica il campo di velocità (riproduce sul fluido la deviazione imposta dalle pale) divenendo responsabile dello scambio di lavoro; la forza parallela genera le perdite; il bloccaggio migliora notevolmente le capacità di previsione sia del coefficiente di lavoro che della portata massima elaborata dalla generica turbomacchina in analisi.

Il modello implementato è stato utilizzato per simulare un sistema accoppiato presa d'aria-fan. Il caso di riferimento è rappresentato da un test in galleria del vento condotto da NASA e GEAE su un modello in scala di fan subsonico. I risultati numerici, espressi in termini di mappe di prestazione, contours e diagrammi spanwise, sono confrontati con i dati sperimentali. L'analisi dei risultati evidenzia che il metodo consente di catturare le caratteristiche globali del campo di moto, tralasciando aspetti locali di interazione fluido-pala. Inoltre l'efficienza massima del fan risulta essere sottostimata, mentre la portata di massa e il coefficiente di lavoro leggermente sovrastimati. Tenendo conto di queste limitazioni, sono proposte alcune possibilità di impiego del metodo in ambito progettuale.

Abstract

Future commercial aircraft concepts feature strong aerodynamic interactions between fan and airframe. In a practical design environment, fast and accurate numerical capabilities are required to capture and characterize these interactions. This thesis presents a non axisymmetric through-flow methodology, often referred to as "body force modeling", in which turbomachinery blade rows are replaced by source terms that reproduce flow turning and losses. A specific body force method, based on lift and drag analogy, is explained and then implemented in a Computational Fluid Dynamics solver. The model consists of three main elements: a normal-to-the-flow force model, a viscous parallel force model and a blade metal blockage model. The normal force produces the turning and thus work exchange, the parallel force generates the losses, metal blockage greatly enhances the accuracy of the flow prediction both in terms of work coefficient and choke mass flow rate. The implemented model is applied to a nacelle-fan configuration to reproduce fan performance maps. The test case is represented by a subsonic fan stage scaled model used in a wind tunnel test conducted by NASA and General Electric Aircraft Engines. The experimental data are reported in this thesis and compared with the numerical model results.

Contents

1	Introduction	1
1.1	Fan-airframe aerodynamic interactions	4
1.1.1	Max climb conditions	4
1.1.2	Crosswind operations	5
1.2	Short Nacelle framework	6
1.3	Boundary layer ingestion	7
1.4	Design challenges	8
1.5	Literature review	9
1.5.1	Explicit body force models	10
1.6	Thesis organization	12
2	Materials and Methods	13
2.1	Body force modeling	13
2.1.1	Governing equations for the body force approach	15
2.1.2	Gong's model	16
2.1.3	Lift/drag model	19
2.1.4	Force decomposition	21
2.1.5	Force field extraction from a blade computation	22
2.1.6	Blockage source terms	23
2.2	Body force implementation	24
2.2.1	Test case: NASA / GEAE Fan stage R4	24
2.2.2	Metal blockage implementation	32
2.2.3	Body force case	36
2.2.4	CFD solver and body force module	37
3	Results and Discussion	43
3.1	Fan performance maps	43
3.2	Contour analysis	47
3.2.1	Mach number ($p_{outlet} = 105000 Pa$)	48
3.2.2	Specific mass flow rate ($p_{outlet} = 105000 Pa$)	49
3.2.3	Total pressure ratio ($p_{outlet} = 105000 Pa$)	50

3.2.4	Total temperature ratio ($p_{outlet} = 105000 Pa$)	51
3.2.5	Mach number ($p_{outlet} = 85000 Pa$)	52
3.2.6	Specific mass flow rate ($p_{outlet} = 85000 Pa$)	53
3.2.7	Total pressure ratio ($p_{outlet} = 85000 Pa$)	54
3.2.8	Total temperature ratio ($p_{outlet} = 85000 Pa$)	55
3.3	Spanwise analysis	56
3.3.1	Specific mass flow rate ($p_{outlet} = 105000 Pa$)	58
3.3.2	Adiabatic efficiency ($p_{outlet} = 105000 Pa$)	58
3.3.3	Swirl angles ($p_{outlet} = 105000 Pa$)	59
3.3.4	Pressure and Flow coefficients ($p_{outlet} = 105000 Pa$)	59
3.3.5	Specific mass flow rate ($p_{outlet} = 85000 Pa$)	60
3.3.6	Adiabatic efficiency ($p_{outlet} = 85000 Pa$)	60
3.3.7	Swirl angles ($p_{outlet} = 85000 Pa$)	61
3.3.8	Pressure and Flow coefficients ($p_{outlet} = 85000 Pa$)	61

4 Conclusions

63

List of Figures

1.1	Trends in bypass ratio (from [9])	3
1.2	Influence of fan diameter on noise and fuel burn (from [9])	3
1.3	Air-intake interactions at max climb (from [13])	4
1.4	Air-intake interactions at crosswind (from [13])	5
1.5	Illustration of the length to diameter ratio of an air intake (from [13])	6
1.6	Aerodynamic interactions between fan and airframe in UHBR engines (from [13]).	7
1.7	Boundary Layer Ingestion concept (from [2]).	8
2.1	Fan stage modeled with body force fields (from [11]).	14
2.2	Normal/parallel force decomposition (from [13]).	14
2.3	Normal force component due to blade loading (from [11]).	17
2.4	Gong's blade passage with forces normal and parallel to local flow direction, $f_{n\delta}$ and f_p (from [11]).	17
2.5	Metal blockage parameter (from [13])	23
2.6	Fan module in the acoustic testing configuration installed on the UHB Drive Rig in the NASA Glenn 9- by 15-Foot Low Speed Wind Tunnel.	26
2.7	Fan performance maps with the Low Noise OGVs installed from [8] (continued).	30
2.7	Fan performance maps with the Low Noise OGVs installed from [8] (concluded).	31
2.8	Blockage test case mesh grids (continued).	32
2.8	Blockage test case mesh grids (concluded).	33
2.9	Axial pressure profiles within the domain for different static pressure values imposed at the outlet.	34
2.10	Mach number contours for simulations with a static pressure value of $p = 78000 Pa$ imposed at the outlet.	35
2.11	Mesh grid used in body force simulations	36
2.12	Solution procedure for density-based solver (from [3]).	40

3.1	Fan performance maps (continued).	46
3.1	Fan performance maps (concluded).	47
3.2	Mach number contours for computations with $p = 105000 Pa$ imposed at the outlet.	48
3.3	Specific mass flow rate contours for computations with $p = 105000 Pa$ imposed at the outlet.	49
3.4	Total pressure ratio contours for computations with $p = 105000 Pa$ imposed at the outlet.	50
3.5	Total temperature ratio contours for computations with $p = 105000 Pa$ imposed at the outlet.	51
3.6	Mach number contours for computations with $p = 85000 Pa$ imposed at the outlet.	52
3.7	Specific mass flow rate contours for computations with $p = 85000 Pa$ imposed at the outlet.	53
3.8	Total pressure ratio contours for computations with $p = 85000 Pa$ imposed at the outlet.	54
3.9	Total temperature ratio contours for computations with $p = 85000 Pa$ imposed at the outlet.	55
3.10	Specific mass flow rate ($p_{outlet} = 105000 Pa$)	58
3.11	Adiabatic efficiency ($p_{outlet} = 105000 Pa$)	58
3.12	Swirl angles ($p_{outlet} = 105000 Pa$)	59
3.13	Pressure and Flow coefficients ($p_{outlet} = 105000 Pa$)	59
3.14	Specific mass flow rate ($p_{outlet} = 85000 Pa$)	60
3.15	Adiabatic efficiency ($p_{outlet} = 85000 Pa$)	60
3.16	Swirl angles ($p_{outlet} = 85000 Pa$)	61
3.17	Pressure and Flow coefficients ($p_{outlet} = 85000 Pa$)	61

List of Tables

2.1	Fan design parameters (from [8])	27
2.2	Geometric and fluid variables (fluid is air considered as an ideal gas)	33
2.3	Theoretical values at the outlet for isentropic outflow solutions	34
2.4	Numerical values computed at the outlet.	35
3.1	Mass-flow averaged results for different outlet pressure values computed one-chord downstream blade trailing edge location.	45

Chapter 1

Introduction

New challenges are emerging for the commercial aircraft industry in recent years, particularly concerning the airplane engine design. In this regard commercial aircraft industry is trying to deal with two specific problems: the reduction of aircraft fuel burn and pollutant emissions on the one hand and the reduction of noise emissions on the other. The reduction of fuel consumption, and so the increasing of engine efficiency, is fundamental to respect environmental constraints and to keep producing competitive air planes. Controlling the noise produced by turbofan engines, since the increased frequency of take-off and landings, has also become a major concern for aircraft owners and airport operators. Therefore, the research is now looking for several and effective solutions to solve these problems and large improvements will be obtained by working on the power-plant and its integration into the aircraft.

The next generation engine for commercial transport aircraft designs higher bypass ratios (BPR) and lower fan pressure ratios (FPR). In order to understand why these two design choices are so important it is useful to consider the following equations.

The propulsive efficiency of a single stream turbojet engine can be written:

$$\eta_{prop} = \frac{2}{1 + \frac{u_e}{u_0}} \quad (1.1)$$

where u_e is the engine exhaust velocity and u_0 is the external flow velocity. The propulsive efficiency is maximum when the exhaust velocity is as close as possible to the external flow velocity.

Thrust can be written:

$$F = \dot{m}(u_e - u_0) \quad (1.2)$$

The analysis of both equations shows that, for a given thrust requirement, it is more efficient to give a small acceleration, $u_e - u_0$, to a large amount

of fluid \dot{m} . In practice, the exhaust velocity decreases with the Fan Pressure Ratio (FPR), and higher mass flow rates can be obtained with larger fan diameters. This explains the current efforts to increase the bypass ratio (BPR) of civil aircraft engines. In addition, significant noise benefits can be achieved in low-speed, low-FPR fan designs by potentially avoiding buzz-saw noise, reducing fan broadband and rotor-stator interaction noise, reducing cabin noise, and enabling steeper take-off profiles for far-field noise reductions due to excess thrust capability at take-off. This design trend is shown in Figures 1.1 and 1.2.

Reductions in fan pressure ratio can be realized for example through low-speed geared fans. The gear system allows the fan rotor and the low spool with the low-pressure compressor (LPC) and low-pressure turbine (LPT) to operate at different rotational speeds. The fan speed can be reduced to limit tip speed and noise while compressor and turbine speeds can be increased to limit stage counts and core weight.

However, this design guideline presents some drawbacks. High bypass and low fan pressure ratios require large engine diameters and larger casing, which lead to increase nacelle weight, overall drag penalties and compounding adverse installation effects on the wing aerodynamics. It is necessary the development of advanced nacelle designs limiting weight and drag penalties. Shorter inlet and exhaust ducts will be required to minimize the impact of larger diameter fans on nacelle weight and drag. However, short inlets have reduced internal diffusion capability and inlet flow distortion effects can be exacerbated, leading to reduced rotor performance, potential stability challenges for the fan and the LPC. In addition, shorter inlets provide reduced fan noise attenuation and shielding opportunities.

On the long term, new propulsion paradigms must be envisioned to further decrease fuel burn. For instance, the Boundary Layer Ingestion (BLI) concept consists in embedding the engines and the airframe together so that the engines ingest a portion of the airframe boundary layer, which decreases wake drag penalties. The aircraft and the engines are fully coupled, as the fans operate under distorted inflow, and as the pressure distributions on the airframe are affected by the fans.

In order to offer a better overview on these concepts a brief review of fan fan-airframe aerodynamic interactions is presented below.

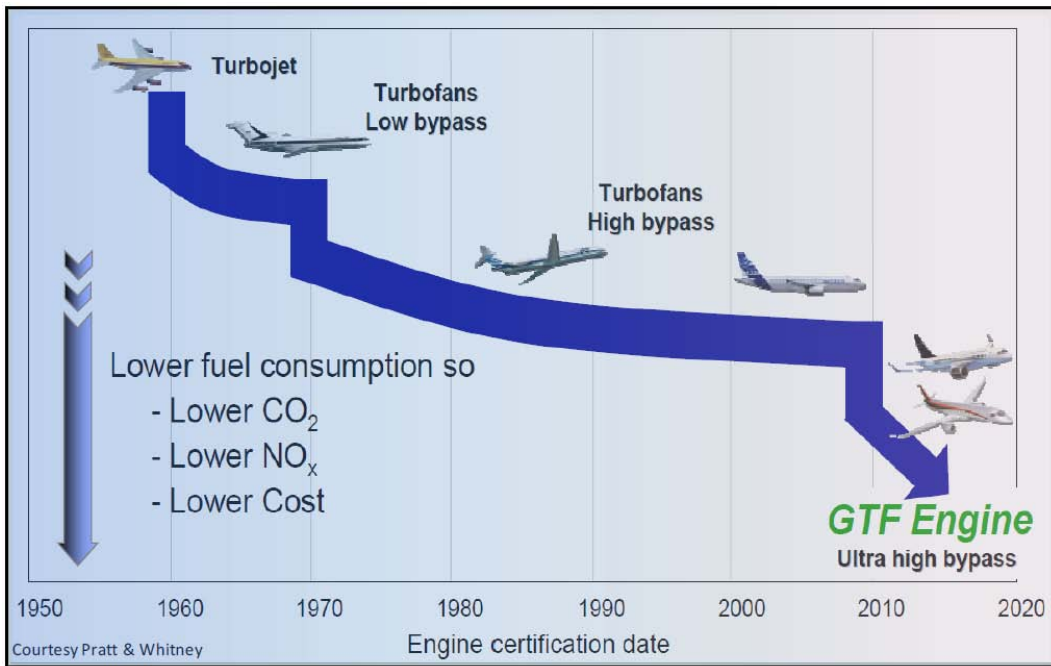


Figure 1.1: Trends in bypass ratio (from [9])

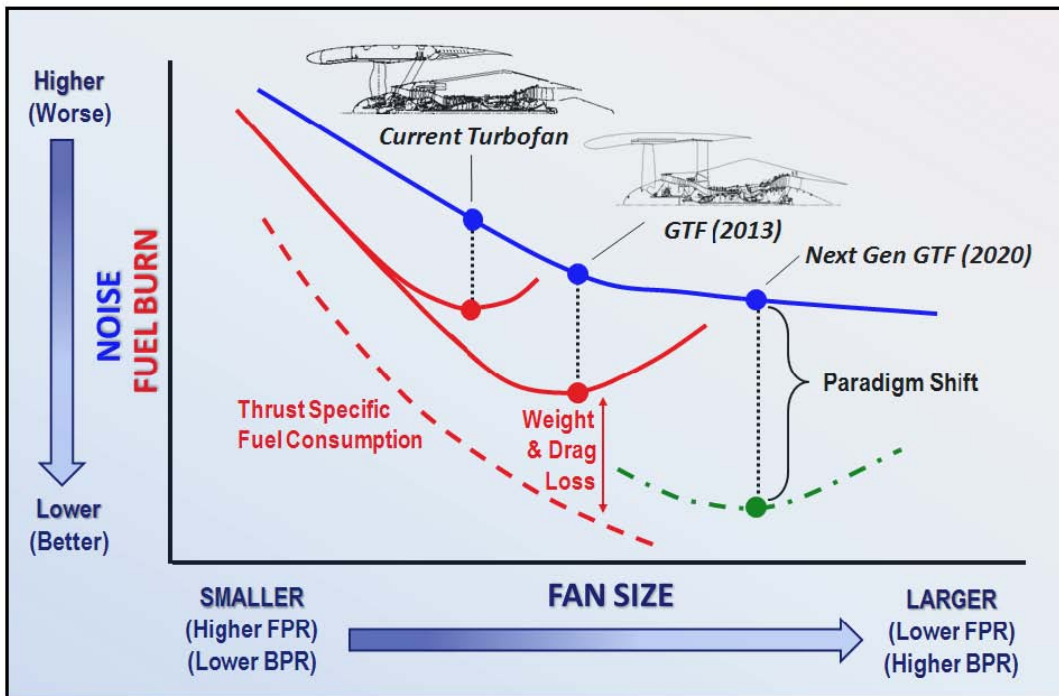


Figure 1.2: Influence of fan diameter on noise and fuel burn (from [9])

1.1 Fan-airframe aerodynamic interactions

The purpose of this section is to describe the engine-airframe aerodynamic interaction challenges that will be encountered on future aircrafts. The first part shortly describes the internal aerodynamics of conventional air intakes, and the potential interactions that occur between fan and intake when the length of the latter is reduced. Then, the BLI concept is presented.

An engine is typically isolated from the rest of the aircraft by a nacelle. An important part of the nacelle is the air intake that delivers air to the engine. From the aerodynamic point of view, the main role of the air intake is to provide the adequate mass flow rate to the fan and Low Pressure Compressor (LPC) stages, with minimum loss and with low-distortion inflow. However, inlet flow distortion cannot be avoided. The amount of distortion at the fan face is a critical aspect for turbo-fan engines and it largely depends from operating conditions. For each engine, a specification in terms of maximum distortion level is given by the engine manufacturer to the intake designer, which must not be exceeded. Two particularly challenging aircraft operating conditions for aerodynamic intake design are presented below.

1.1.1 Max climb conditions

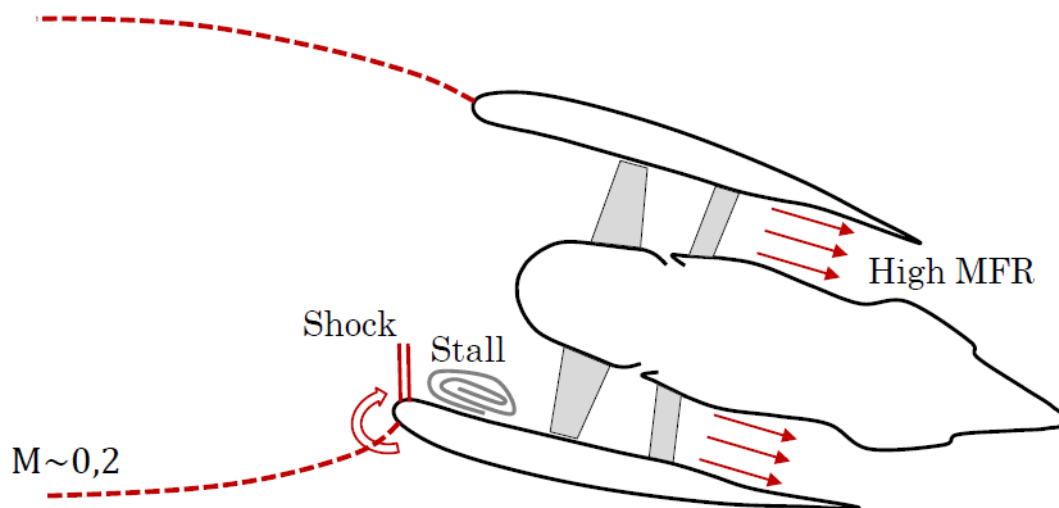


Figure 1.3: Air-intake interactions at max climb (from [13])

In some situations, an aircraft must be able to quickly gain altitude, to avoid an obstacle for instance. Due to the upstream deflection of the wing, the air intake is locally subject to high angle of attack (AOA), which could

lead to flow separation on the lower intake lip, as shown in Figure 1.3. As the flow goes around the lower lip, it is accelerated until a normal shock appears and that shock could trigger flow separation in the air intake. Consequently, the distortion upstream of the fan may be high enough to strongly deteriorate the fan and LPC performance and reduce their stall margin. The intake is therefore designed to avoid separation up to the aircraft C_{Lmax} conditions.

1.1.2 Crosswind operations

When the aircraft is operated on the ground before take-off, severe cross wind conditions may impact the operation of the engine, as shown in Figure 1.4.

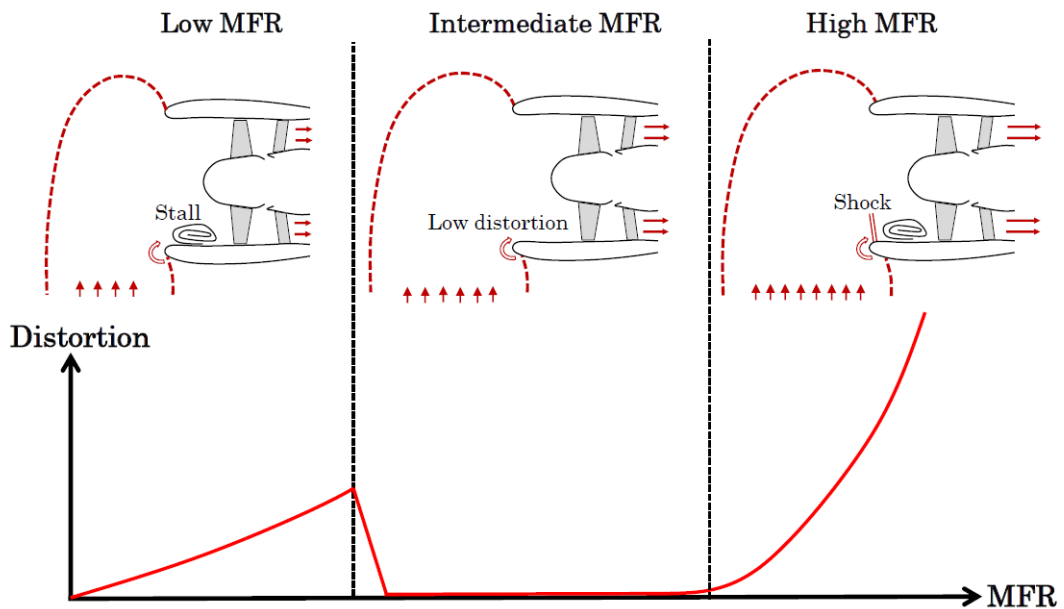


Figure 1.4: Air-intake interactions at crosswind (from [13])

At low values of mass flow rates (MFR), the flow has not enough momentum to follow the lip curvature and the intake flow is separated. As the mass flow rate increases, the stall region disappears, and the distortion level becomes lower. Finally, at high mass flow rates, a normal shock appears on the lip, which can lead to flow separation and high distortion levels at the fan face, similarly to what happens at max climb.

1.2 Short Nacelle framework

Future turbofan engines, as stated at the beginning, will feature larger fan diameter and lower FPR to reach higher propulsive efficiency, but this comes at the expense of increased casing diameters and thus increased nacelle drag and weight. One solution is to reduce the length of the air intake, or more specifically its length to diameter ratio, L/D , as shown in Figure 1.5.

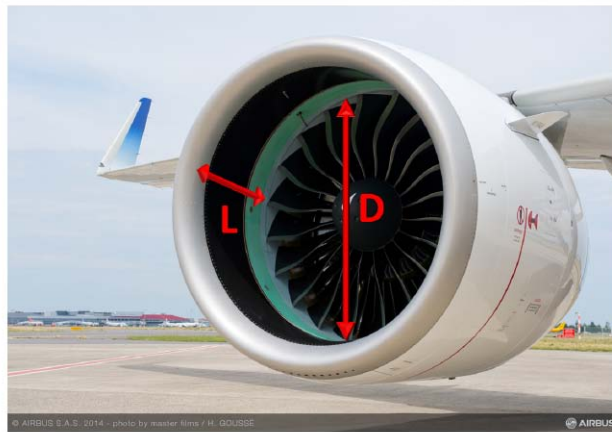


Figure 1.5: Illustration of the length to diameter ratio of an air intake (from [13])

However, reducing the length of an air intake is not trivial for several aspects, first among all the inlet flow distortion. The aerodynamics of both intake and fan are affected. On one hand the fan has a strong upstream influence on distortion: it is proved fan reduces upstream distortion and delays the onset of separation for high AOA conditions. On the other hand, a short intake design does not completely suppress the velocity distortion at the fan face, which decreases the fan efficiency.

The recommended inlet length for maximized engine propulsive efficiency is suggested by Peters [11] to be an L/D between 0.25 and 0.4. A candidate $L/D = 0.25$ configuration was demonstrated to come to within 0.01 of reaching the propulsive efficiency provided by the $L/D = 0.5$ baseline case. However, at off-design operating conditions the rotor performance is significantly degraded due to the increased incidence distortion at the fan face. At the upper end of the recommended inlet L/D range, incidence distortion and resulting rotor efficiency penalties are mitigated while nacelle drag increases due to the larger surface area.

Another important design parameter is the shape, or thickness, of inlet lips. Thin inlet shapes are preferred at cruise to limit nacelle wave drag

and mitigate the local increase in stream-wise Mach number at the fan face. However, thick inlet contours are needed at off design to avoid regions of separated inlet flow. Shorter inlets also imply logistic and noise problems: the distance between fan, OGV, bifurcation and exhaust may be reduced, such as the room available for critical systems (i.e. anti-icing devices), leading to increased interactions between those elements; the potential for aeroacoustic shielding will also be penalized. Lastly because of the decrease in FPR, it is more likely that the fan nozzle will be unchoked even at maximum mass flow rate, enabling some interactions between the fan and downstream airframe components such as the wings and flaps. All these problems are pictured in Figure 1.6

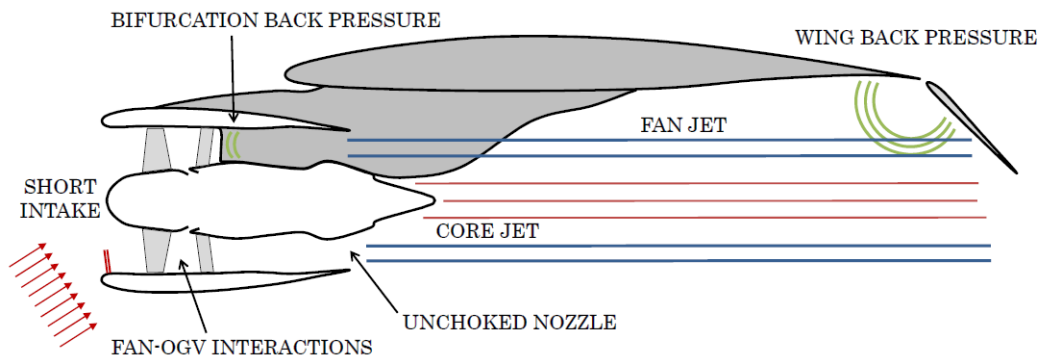


Figure 1.6: Aerodynamic interactions between fan and airframe in UHBR engines (from [13]).

It is clear that short inlets design involves trade-offs between the performance at cruise and off design, but it also requires new simulation strategies and methods to capture effectively the increased interactions between different engine items.

1.3 Boundary layer ingestion

While short nacelles allow to mitigate the drawbacks of larger engines, boundary layer ingestion is a promising concept that consists in ingesting the airframe boundary layer with the engines rather than free stream air, to reduce wake drag penalties and increase the propulsive efficiency. The design configuration for this kind of aircraft is presented in Figure 1.7.

An important challenge for the practical application of this concept is that the fans and the airframe strongly interact with each other. The fans alter the pressure distributions on the airframe, which modifies lift and drag

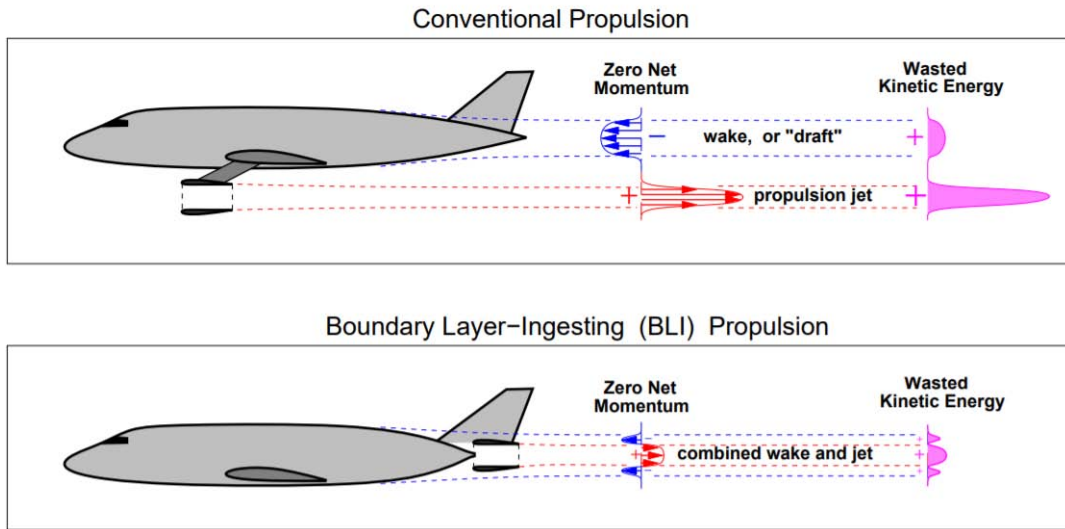


Figure 1.7: Boundary Layer Ingestion concept (from [2]).

and thus thrust requirements. Reciprocally, because of the boundary layer ingestion, the fans receive distorted inflow, fan efficiency reductions of about 1% to 2% relatively to uniform inflow. On the other hand, an estimated increase in 0,8% fuel burn per 1% decrease in fan cruise efficiency was found.

1.4 Design challenges

In the previous sections challenging design solutions, UHBR and BLI, have been presented, paying attention to the operating conditions and related problems.

As far as their design concern new simulation strategies and methods are now necessary to capture effectively the increased interactions between different engine items in the UHBR or between engine and aircraft in BLI configurations. The onset of flow separation at off-design operating condition with large angles of attack is one of the critical considerations in the design of subsonic inlets. In conventional propulsion engines are isolated from the aircraft by a long inlet nacelle. In this configuration fan and nacelle inlet can be considered and simulated as two disconnected items, so through-flow nacelle models are enough to solve the problem. However, these models do not account for the effects induced by the rotor including blockage, swirl, and suction. A coupled fan-nacelle design approach is required as the inlet length

is reduced and the interaction between inlet flow and fan stage increases.

In the past, several numerical studies using potential flow and Euler analyses, or two-dimensional actuator disk models (AD) with a Navier-Stokes code were conducted to simulate the flow through the fan rotor. However, potential flow simulations are limited to subsonic, non-separated flows; Euler calculations can be used in sub- and supersonic conditions but are also limited to attached flows; actuator disk misses important flow features, such as choke and mass flow redistribution within the blade row.

Direct CFD simulations are another approach but full-annulus domains are needed to capture the once-per-revolution inlet distortion patterns and unsteady computations without mixing planes are required to assess the distortion transfer through the fan stage. Furthermore, a detailed geometry of the fan blades is required and a fine mesh is necessary to capture wall flows. The large computational resources associated with full-annulus unsteady RANS (URANS) calculations render the direct CFD approach unsuitable in the design phase for the parametric exploration of coupled inlet-fan systems. Therefore, the next chapter explores a class of reduced order methods, known as Body Force methods, in which the computational cost is further reduced.

1.5 Literature review

This section reviews a class of through-flow models for turbomachinery in which the blades are not directly included in the CFD simulation but considered using work and loss forcing terms. In these models, called Body Force Methods (BFM), the effect of a turbomachinery blade row is simulated through a source terms distribution amounting to the same effect, in terms of turning and losses, that a solid blade produces on the fluid. This new modeling approach is due to Marble, who in 1964 [10] built an axisymmetric representation of a blade row, assuming an infinite number of blades, and taking their effects into account by adding body forces to the equations of motion. Thanks to this representation Marble derived thermodynamic relations linking the blade forces to the total enthalpy change and to the production of entropy within the blade row.

In literature several through-flow methods, inspired by Marble's studies, are present and generally they can be divided in two main categories:

- Axisymmetric through-flow methods
- Non axisymmetric through-flow methods

Non-axisymmetric through-flow methods for 3D analysis can be in turn divided into several groups

- Explicit, physics-based body-force models
- Interpolation-based models
- Semi-explicit models, intermediate between both previous approaches
- Implicit approaches based on deviation and loss correlations

In explicit body force approaches a physics-based model is derived for the blade force. The deviation and the losses are then a result of the computation. The blade force is usually computed locally and only depends on the local flow conditions. The effect of inlet distortion is thus naturally captured. In interpolation-based approaches assume a dependency between the body forces and local flow variables such as the flow coefficient or the relative Mach number. Then, a response surface or a look-up table is built from a body-force database, which allows the body forces to locally respond to varying inflow conditions. In Semi-explicit approaches involve a physics-based relationship between the body forces and key quantities such as the gradient of entropy or the gradient of tangential velocity. However, these quantities are not modeled but retrieved using, as for the interpolated body force approach, a look-up table or a response surface.

Implicit approaches do not explicitly link the body force responsible for turning to the flow field. The blade force is computed at each iteration to force the streamlines along a mean flow path that is defined using the blade camber surface and a deviation distribution. Forces are thus a result of the computation.

For this study the 3D explicit body force approach has been selected as reference and some studies of authors that used this approach in the past are presented below.

1.5.1 Explicit body force models

Gong's model An important contribution is that of Gong et al. [5] in 1998, who presented a computational model for low-speed axial compressor stall inception. In his PhD dissertation, Gong [4] applied it to study the response of the NASA stage rotor 35 to inlet distortion. To derive the model, Gong used Marble's decomposition of the blade force into a normal and a parallel component. The normal component is itself divided into a pressure gradient-based term, which represents the blade loading, and a deviation-based term,

which responds to the local deviation. Both components rely on calibration coefficients that Gong estimated with empirical correlations. Hsiao et al. [7] later applied Gong’s formulation to a powered nacelle, focusing on the effect of the fan on inlet flow separation. Plas et al. [12] used Gong’s model to assess the performance of an embedded propulsion system in the presence of distortion due to boundary layer ingestion. The main advantage of Gong’s method is that the body forces depend on the local flow field, allowing the model to respond to flow perturbations on a physical basis.

Peters’s model Peters et al. [11] used an improved version of Gong’s model to find an optimal air-intake length. The modifications of the model consisted in the inclusion of off-design losses in the parallel force and the addition of a radial component to the normal force. The model was calibrated using RANS mixing-plane computations and it was able to accurately reproduce results obtained with full annulus unsteady computations. But the process to calibrate the model was heavy and required a manual intervention.

However, Peters showed that Gong’s formulation does not allow to capture the local streamline curvature in a blade passage, and he mentioned the lack of a model for metal blockage in Gong’s body force approach.

Hall’s model Hall [6] later proposed an inviscid (normal force only), first-principle based incompressible body force model that does not rely on empirical coefficients. The model was used to study the interaction of a fan with a BLI-type inlet distortion. However, his formulation did not include any model for the loss, and it was restricted to incompressible flows only. Furthermore, it did not use a model for metal blockage, which is required to capture the choke mass flow rate of a transonic fan stage (for instance at max climb conditions).

Thollet’s lift/drag model In 2017 Thollet proposed a different modeling approach to address Gong’s model limitations [13]. The approach is derived based on a lift/drag analogy of a wing for the normal and parallel force components respectively. Additional source terms are added to the RANS equations to capture metal blockage. This formulation requires calibration coefficients, but the calibration process is more robust than for Gong’s model with Peters’ modifications. The model was successfully employed to reproduce NASA R4 fan stage speed lines and it was able to capture the choke mass flow rates, although it underestimated the peak efficiency.

1.6 Thesis organization

The second chapter of this thesis is dedicated to the body force modeling. Gong's model is considered as reference for explicit body force methods and then the Thollet lift/drag approach is exposed. An implementation in a commercial CFD solver is proposed and the experimental test case used to validate the numerical model is described.

In the third chapter the numerical results are presented and discussed. The last chapter reports the conclusions of this study.

Chapter 2

Materials and Methods

2.1 Body force modeling

This chapter describes an explicit body force model which was used, after the implementation in a fluid dynamics solver, to capture the performance of a subsonic fan stage.

In general, a Body Force Method (BFM) for turbomachinery is a through-flow model where the effect of a blade row is simulated through a force distribution amounting to the same effect that a solid blade has on the fluid. The blades are replaced by a body force field in the swept volume of the actual blade row, as illustrated in Figure 2.1.

Following Marble's foundational work, the blade forces per unit mass, \vec{f} , are divided into a force component normal to the flow and a force component parallel to the flow in the blade row frame of reference, denoted by f_n and f_p , respectively, as pictured in Figure 2.2. The normal force represents the blade loading and provides the flow turning while the parallel force is responsible for generating the viscous losses in the blade row.

Inside the body force field region, source terms are added to the momentum and energy equations to produce the same pitch wise-averaged flow turning, enthalpy change, and entropy generation as the blades. Metal blockage must also be reproduced. Replacing the discrete blades with body force distributions leads to simplified grid topologies and reductions in grid point counts since fine mesh resolutions near the blade surfaces are no longer needed.

A body force approach requires two steps: the first one is to extract the blade forces which recreate the axisymmetric mean flow field; the second step is to define the relationship which governs how the body force locally responds to changes in the flow.

A possible solution is to extract the body force field from the blade sur-

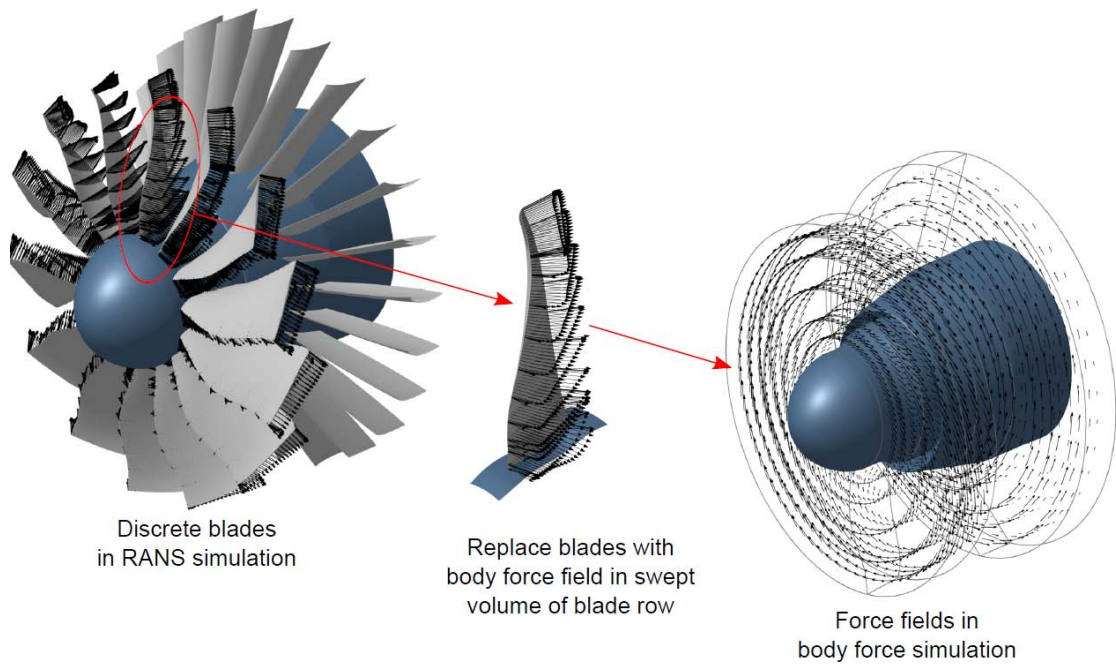


Figure 2.1: Fan stage modeled with body force fields (from [11]).

face pressures and averaged (or "smeared out") over a blade passage while the dependency of the body force on the local flow is derived from analytical formulations. This approach, originally developed by Gong and then improved by Thollet [13], has taken as reference in this thesis.

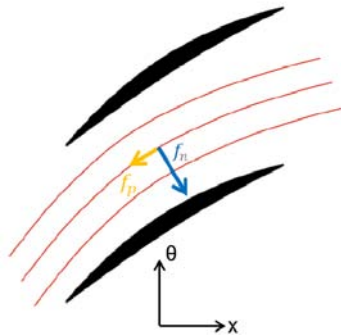


Figure 2.2: Normal/parallel force decomposition (from [13]).

2.1.1 Governing equations for the body force approach

For flow in the blade rows, the full three-dimensional unsteady Euler equations with body forces in cylindrical coordinates x, r, θ are given by

$$\begin{aligned} \frac{\partial}{\partial t} \begin{bmatrix} r\rho \\ r\rho V_x \\ r\rho V_r \\ r\rho V_\theta \\ r\rho e_t \end{bmatrix} + \frac{\partial}{\partial x} \begin{bmatrix} r\rho V_x \\ r\rho V_x^2 + rp \\ r\rho V_x V_r \\ r\rho V_x V_\theta \\ rV_x(\rho e_t + p) \end{bmatrix} + \frac{\partial}{\partial r} \begin{bmatrix} r\rho V_r \\ r\rho V_r V_x \\ r\rho V_r^2 + rp \\ r\rho V_r V_\theta \\ rV_r(\rho e_t + p) \end{bmatrix} + \frac{\partial}{\partial \theta} \begin{bmatrix} \rho V_\theta \\ \rho V_\theta V_x \\ \rho V_\theta V_r \\ \rho V_\theta^2 + p \\ V_\theta(\rho e_t + p) \end{bmatrix} \\ = \begin{bmatrix} 0 \\ rF_x \\ \rho V_\theta^2 + p + rF_r \\ -\rho V_r V_\theta + rF_\theta \\ r(\vec{F} \cdot \vec{V} + \dot{Q}) \end{bmatrix} \end{aligned} \quad (2.1)$$

where ρ is the fluid density, $\vec{V} = (V_x, V_r, V_\theta)^T$ is the velocity vector, p is the static pressure and e_t is the absolute stagnation internal energy per unit mass, such that the stagnation enthalpy is given by $h_t = e_t + \frac{V^2}{2}$. The body force source terms (in units of force per unit of volume) and the heat source term (in units of heat release per unit of volume) are denoted by $\vec{F} = (F_x, F_r, F_\theta) = \rho(f_x, f_r, f_\theta)^T$ and \dot{Q} , respectively. If there is no heat source in the fluid, the energy source term in 2.1, $\vec{F} \cdot \vec{V} + \dot{Q}$, reduces to the work done by the body forces on the flow

$$W_{source} = \vec{F} \cdot \vec{V} + \dot{Q} = F_\theta \Omega r \quad (2.2)$$

where Ω is the blade row rotational speed. The body force $\vec{F} = (F_x, F_r, F_\theta)$ represents the influence of the blade row on the flow and varies both with spatial location in the blade row and operating condition.

Following Marble's analysis [33], relations can be derived to demonstrate how the body forces change the enthalpy and entropy of the flow. Substituting for the pressure gradient in the Gibbs equation, $Tds = dh - \frac{1}{\rho} dp$, using the steady inviscid momentum equations in cylindrical coordinates yields

$$W_m \frac{\partial h_t}{\partial m} - F_\theta \Omega r = TW_m \frac{\partial s}{\partial m} + \vec{W} \cdot \vec{F} \quad (2.3)$$

where m is in the direction of a meridional streamline, \vec{W} is the relative velocity vector, s is the entropy, and T denotes the static temperature. The

parallel body force component is parallel to the relative flow, $\vec{W} \cdot \vec{F} = WF_p$. The circumferential momentum equation and the Euler turbine equation can be combined to give

$$\frac{\partial h_t}{\partial m} = \frac{F_\theta \Omega r}{W_m} \quad (2.4)$$

Equation 2.4 implies that the rate of change of stagnation enthalpy along a meridional streamline is proportional to the rate at which the torque applied by the circumferential body force does work on the fluid. Combining equations 2.4 and 2.3 yields

$$\frac{\partial s}{\partial m} = -\frac{W}{W_m T} F_p \quad (2.5)$$

Equation 2.5 states that the changes in entropy along a meridional streamline are due to the parallel force which accounts for the losses by the viscous shear stresses.

2.1.2 Gong's model

Basis of the method

Before describing Thollet's method the classic Gong's model is briefly presented in this section. Gong used Marble's decomposition of the blade force into a normal and a parallel component to relative flow velocity. The normal component is itself divided into a pressure gradient-based term, which represents the blade loading, and a deviation-based term, which responds to the local deviation

$$\vec{f}_n = \vec{f}_{n\nabla p} + \vec{f}_{n\delta} \quad (2.6)$$

In order to discover the functional dependence of the two normal force components in 2.6 on the local flow conditions in the blade row frame of reference, Gong used two different approaches.

A force balance for a two-dimensional blade channel with discrete blades was employed to derive the body force due to blade loading, $\vec{f}_{n\nabla p}$. The response of the normal force $\vec{f}_{n\delta}$ due to differences between the relative streamline and the local camber line, i.e. changes in deviation, was derived based on the cross-passage momentum balance in a staggered channel. This two approaches are illustrated in Figures 2.3 and 2.4.

The resulting formulation for the normal force magnitude is given by

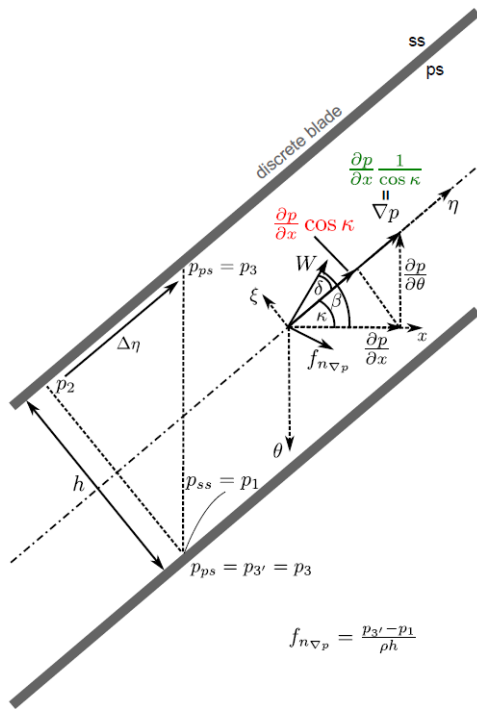


Figure 2.3: Normal force component due to blade loading (from [11]).

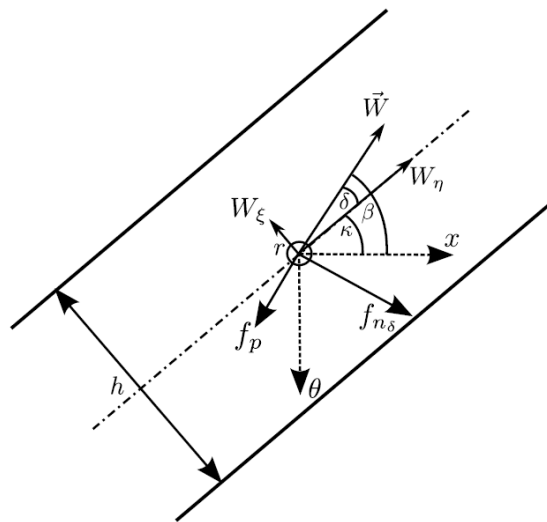


Figure 2.4: Gong's blade passage with forces normal and parallel to local flow direction, $f_{n\delta}$ and f_p (from [11]).

$$f_n = f_{n\nabla p} + f_{n\delta} = \frac{1}{\rho} \frac{\partial p}{\partial x} \frac{\sin\kappa}{\cos^2\kappa} + \frac{K_n(x, r)}{h} W^2 \frac{1}{2} \sin(2\delta) \quad (2.7)$$

where $\kappa = \kappa(x, r)$ denotes the local blade metal angle, h is the staggered spacing between two blades, and $\frac{\partial p}{\partial x}$ is the axial component of the pressure gradient. The deviation angle is defined as the angle between the local relative flow direction and the local camber line, $\delta = \beta - \kappa$. The normal force component due to changes in the deviation includes a scaling function $K_n = K_n(x, r)$, which is labelled the normal body force coefficient. The body force coefficient can be viewed as the empirical link between force and flow field and must be determined before a body force simulation can be carried out, either from experiments or computations.

As far as it concerns the parallel component of the force, which represents the viscous losses and acts opposite to the relative flow direction, Gong proposed, in analogy with an airfoil drag relationship, the following equation

$$f_p = \frac{K_p(x, r)}{h} W^2 \quad (2.8)$$

If the parallel force magnitude and the velocity in the blade domain are known from experimental data, empirical correlations, or CFD results, the parallel body force coefficient K_p can be calculated from Equation 2.8.

Limitations of the method

This model, that was used by Gong in his PhD thesis to compressor stability investigations, presents the following drawbacks:

- Blade metal and aerodynamic blockage are not accounted for thus the model is not able to correctly predict work and choke mass flow rate.
- The radial force and velocity components due to blade lean were assumed negligible and a constant value was originally assigned to the coefficient K_p by Gong. Not considering radial components of the normal blade force leads to an underestimation of the off-design losses as proved by Peters [11].

Especially regarding the second point, some authors provided different alternatives to set the problem. Peters [11] added a radial component to the normal force using the blade lean angle and introduced a dependency of the coefficient K_p on the relative Mach number to form a loss bucket and account for off-design losses. While the resulting model gave accurate results the calibration process was heavy. Thollet [13] later suggested an improved

version of Peters’s method but the calibration process was not robust and sometimes led to localized errors. Furthermore, the new formulation of K_p was not enough to accurately capture off-design losses.

For these reasons Gong’s model is not taken as reference for this study but it was nevertheless exposed since it allows to clearly understand the key points of explicit body force methods. An alternative approach is proposed in the next section.

2.1.3 Lift/drag model

Basis of the method

This model, due to Thollet [13], is the foundation of this work. The approach is derived-based on a lift/drag analogy for the normal and parallel force components respectively:

$$f_n = \frac{2\pi\sigma}{h} W^2 (\beta - \beta_0) \quad (2.9)$$

$$f_p = \frac{K_p}{h} W^2 \quad (2.10)$$

$$K_p = K_p^{\eta_{max}} + 2\pi\sigma (\beta - \beta_{\eta_{max}})^2 \quad (2.11)$$

$$h = \frac{2\pi r \cos\beta_m}{Z} \quad (2.12)$$

where σ is the blade row solidity, h is the scaled pitch, W is the relative velocity modulus, β is the relative velocity angle ($\beta = \text{atan2}(W_\theta/W_x)$) and Z is the blade number. The model is based on three calibration coefficients, namely β_0 , $K_p^{\eta_{max}}$ and $\beta_{\eta_{max}}$.

According to Thollet this formulation is due to the observation the results given by Gong’s model are more sensitive to variations of the blade metal angle than to variations of K_n .

Parallel force component contains a term that aims at naturally capturing off-design losses, with the idea that high deviation angles correspond to thick boundary layers and to cases with separated regions that generate large amounts of losses. With this approach, the coefficient $K_p^{\eta_{max}}$ sets the minimum amount of losses, i.e. the maximum efficiency losses, and off-design losses are triggered by flow angle deviations from this operating point.

Therefore, this model is well suited to obtain a performance map of a subsonic fan stage: it can be calibrated for each speed line from the operating point at peak efficiency only, from which the three calibration coefficients must be derived, at each meridional grid point, by inverting the above relations (once the normal and parallel forces have been properly extracted).

Application of an offset in the normal force

A problem was found by Thollet carrying out 3D simulations at high rotational speeds of a subsonic fan. The model overestimates the choke mass flow rate and the work coefficient in the rotor, because the flow turning is too high near the leading edge of the rotor. For this reason, Thollet suggested a shape function C (equation 2.14) that off sets the β_0 distribution near the leading edge of the rotor. The function is equal to $1 + C_0$ at the leading edge, then decreases linearly to 1 at mid-chord and remains constant afterwards, where C_0 is the offset constant with values between 0.01 and 0.05, depending on the case.

The new expression for the normal force component is

$$f_n = \frac{2\pi\sigma}{h} W^2 (\beta - C(x) \beta_0) \quad (2.13)$$

where the shape function is

$$C(x) = \max \left\{ 1 + C_0 \left(1 - 2 \frac{x - x_{LE}}{x_{TE} - x_{LE}} \right), 1 \right\} \quad (2.14)$$

This modification improves the prediction of work coefficient over the speed line and allows to capture the choke mass flow rate more accurately, but a trial and error procedure is required to find the value of C_0 that gives the correct choke mass flow rate. In addition, the maximum efficiency is slightly underestimated when the offset is applied, as the flow angle distribution in the body force simulation differs from the one in the blade computation at maximum efficiency.

2.1.4 Force decomposition

The model presented above provides only the modulus of the normal and parallel force. Its application as a source term in RANS equations requires a proper decomposition along the axis, either in cartesian or cylindrical coordinates, according to the solver employed (most 3D general purpose commercial solvers are written in cartesian components, e.g. ANSYS CFX, ANSYS Fluent, STAR-CCD, NUMECA, etc.).

Parallel force

The parallel force must increase entropy and is regarded as a drag, acting along the relative velocity direction, but with opposite verse. It is readily seen that

$$\vec{f}_p = -|f_p| \frac{\vec{W}}{\|\vec{W}\|} \quad (2.15)$$

Normal Force

Differently from parallel component, there is no unique normal direction for a 3D vector. Care must be taken when distributing the force in its three axis components, since improper decomposition may vary its modulus. To do that it is convenient to use a cylindrical coordinate frame first, which springs naturally for turbomachinery. In this coordinate system normal force presents generally three components

$$\vec{f}_n = \{f_{n,r}, f_{n,\theta}, f_{n,z}\} \quad (2.16)$$

Once distributed the normal force onto the three cylindrical axes, we may want to convert it into cartesian components when dealing with cartesian solvers. This is straightforward using again rotation matrix:

$$\vec{f}_n = \begin{bmatrix} f_{n,x} \\ f_{n,y} \\ f_{n,z} \end{bmatrix} = \begin{bmatrix} \cos(\phi) & -\sin(\phi) & 0 \\ \sin(\phi) & \cos(\phi) & 0 \\ 0 & 0 & 1 \end{bmatrix} \begin{bmatrix} f_{n,r} \\ f_{n,\theta} \\ f_{n,z} \end{bmatrix} \quad (2.17)$$

where $\phi = \text{atan2}(y, x)$ (x and y are the center coordinates of each cell within the mesh grid).

2.1.5 Force field extraction from a blade computation

As discussed in Section 1.1.3, the Lift/Drag model provided by Thollet[13] requires three calibration coefficients, namely β_0 , $K_p^{\eta_{max}}$ and $\beta_{\eta_{max}}$. While the last is simply the β angle at peak efficiency, the others are both derived by inverting the relations (2.9) and (2.10) at peak efficiency for a 3D blade simulation, once the normal and parallel forces have been properly extracted.

Several procedures are proposed in literature to extract the force field from a blade computation and one is discussed below.

Force field extraction from thermodynamic quantities

A possibility to extract body forces from a blade computation is to apply Marble's relationships, which relate the parallel and tangential force to the entropy gradient and to stagnation enthalpy gradient respectively, as shown in equations (2.4) and (2.5). Spatial derivatives can be computed using a second order centered finite difference method at the cell centers, where the flux variables and thermodynamic quantities have been averaged. The main advantage of this approach is that it can easily be implemented within an existing software that computes pitch-averaged flows.

In according to [13] the entropy can be also assumed to vary linearly between the leading and trailing edge of the blade, and the streamlines to remain at constant relative span, which allows to approximate the entropy gradient by

$$\frac{\partial s}{\partial m} = \frac{\Delta s}{\Delta m} = \frac{s_{TE} - s_{LE}}{\sqrt{(x_{TE} - x_{LE}) + (r_{TE} - r_{LE})}} \quad (2.18)$$

This allows to simplify the parallel force extraction process and to smooth the parallel force distribution. It also allows to define a body force model for the parallel force calibrated with radial profiles of total pressure and total temperature upstream and downstream of the blade row, either from experimental or CFD data.

The main advantage of this thermodynamics-based approach is its ability to capture all the mechanisms responsible for deviation and loss, including wakes and secondary flows. However, its main drawback is that it can lead to spurious variations of the axial blade force near the hub and the shroud. In fact, to retrieve the axial component of the blade force, the following relationship must be used:

$$f_x = f_{px} - (f_\theta - f_{p\theta}) \frac{W_\theta}{W_x} \quad (2.19)$$

When the relative flow is almost tangential, equation (2.19) gives spurious oscillations for the axial force. Another limitation is that the approach captures the entropy elevation due to the friction on both the blade walls and the end-walls. In a RANS body force computation, the losses on the end-wall are already captured, which leads to an overestimation of the losses in the hub and tip regions.

It is important to underline this method has been qualitatively mentioned for information only. The procedure is outside the objectives of the present work, in which the computed calibration coefficients are an input data as discussed in next sections.

2.1.6 Blockage source terms

In order to capture the correct choke mass flow rate, it is necessary to deal with blade blockage. Excluding the aerodynamic blockage, the lift and drag model requires additional source terms to simulate the effects of blade metal blockage. Metal blockage b is a factor defined by equation (2.20) and illustrated in Figure 2.5

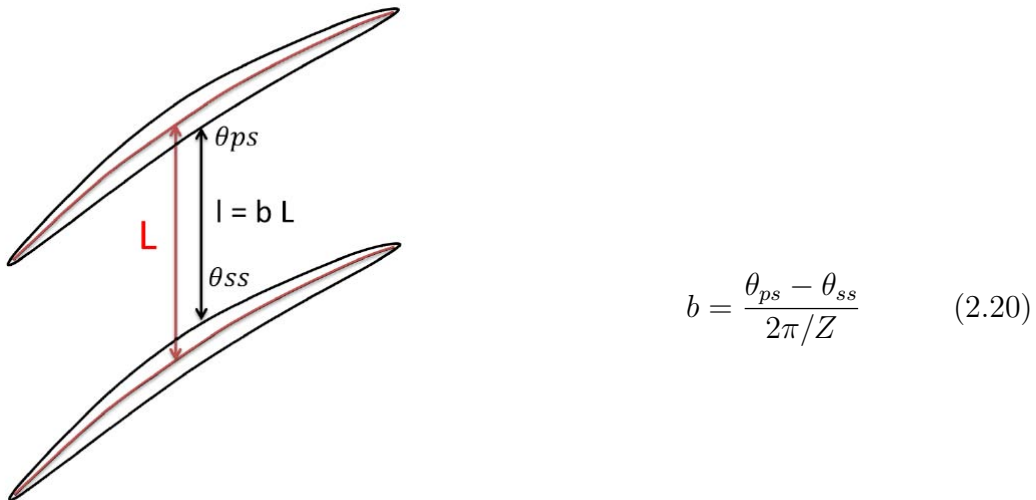


Figure 2.5: Metal blockage parameter (from [13])

In (2.20) Z is the number of blades, θ_{ps} and θ_{ss} are the angular coordinates of blade pressure side and blade suction side respectively. It is clear from (2.20) that b is comprised in $[0, 1]$: the upper limit of the range represents the absence of blading (it is the condition to be imposed on cells out of blade

domain in CFD computations) while the lower one is a limit condition in which solid materials fills the entire passage section (it is the condition to be imposed on walls in CFD computations).

Accounting for blockage the governing equations (2.1) can be modified as follow:

$$\frac{\partial \rho}{\partial t} + \text{div} \left(\rho \vec{V} \right) = -\frac{1}{b} \left(\rho \vec{V} \cdot \vec{\nabla} b \right) \quad (2.21)$$

$$\frac{\partial \rho \vec{V}}{\partial t} + \text{div} \left(\rho \vec{V} \vec{V}^t \right) + \vec{\nabla} p = \rho \vec{f} - \frac{1}{b} \left(\rho \vec{V} \cdot \vec{\nabla} b \right) \vec{V} \quad (2.22)$$

$$\frac{\partial \rho e_t}{\partial t} + \text{div} \left(\rho h_t \vec{V} + \vec{q} \right) = \rho \Omega r f_\theta - \frac{1}{b} \left(\rho h_t \vec{V} \cdot \vec{\nabla} b \right) \quad (2.23)$$

Blockage has become an additional source term which does not change conservative variables and their fluxes, allowing a less intrusive implementation into an existing solver.

2.2 Body force implementation

In this section the implementation of the lift/drag model in an existing solver is presented. The key points of this implementation are:

- A quasi-steady assumption allows to perform steady computations.
- The blade forces that produce turning and losses are computed with the formulations mentioned in the previous section.
- Metal blockage effects are considered with specific source terms.
- The source terms are computed within a C module and a coupling is set up with the CFD solver to consider these source terms.

This model is used in this study to capture the performance of a subsonic fan stage, NASA / GEAE Fan stage R4, which is now described.

2.2.1 Test case: NASA / GEAE Fan stage R4

In order to more fully understand the noise sources and noise generation mechanisms in a modern turbofan engine, in 1999 NASA and General Electric Aircraft Engines conducted a scale model wind tunnel test of a turbofan simulator, called the ‘‘Source Diagnostic Test’’ (SDT) [8].

For this test, the bypass stage portion of a medium pressure ratio, high bypass ratio turbofan engine representative of a current technology product was simulated in approximately 1/5 model scale. The test was conducted in the NASA Glenn Research Center 9- by 15-Foot Low Speed Wind Tunnel. The aerodynamic test objectives were the following ones:

1. Establish the baseline aerodynamic performance level for the scale model fan selected.
2. Assess the aerodynamic performance levels of the fan stage with each of the three low noise outlet guide vane designs by testing each of them with the same fan at the same operating conditions.
3. Determine the effect of the outlet guide vane configuration on the fan baseline performance.
4. Obtain details of the outlet guide vane performance using detailed flow field surveys on and around the outlet guide vanes.

For the purpose of this thesis just the first objective is relevant, and it represents the experimental test case for all the numerical simulations that have been carried out. The description of the experiment and the results regarding the fan are presented below.

Test apparatus

NASA Glenn Research Center Low Speed Wind Tunnel The 9- by 15-Foot Low Speed Wind Tunnel is an anechoic wind tunnel facility located at the NASA Glenn Research Center in Cleveland, Ohio. The facility is operated as an open loop, continuous flow wind tunnel at atmospheric pressure conditions. The wind tunnel can produce velocities in the test section from Mach number 0.0 to 0.23 and very low free-stream turbulence and distortion levels, making it ideal for acoustic testing of propulsion systems.

Turbofan Propulsion Simulator A propulsion simulator called the NASA Glenn Ultra High Bypass (UHB) Drive Rig was used to power the model fan test article. A four-stage air turbine generates the power that is supplied to the fan model through a common shaft connection.

Fan Module The fan module was designed and built by GEAE with partial funding from NASA. It consisted of the fan, the outlet guide vanes (OGVs) and a flight-type nacelle, which included a flight-type inlet, a cowl and a fixed-area, flight-type nozzle. The fan module and UHB rig are depicted in figure.

The fan used for this test was 22-inch diameter and had 22 individual, wide chord blades. It represented a medium pressure ratio bypass fan design, with a stage design point pressure ratio of 1.47 at a model corrected speed of 12,657 RPMc, which corresponds to a design point fan tip speed of 1,215 feet per second. Table 2.1 provides a summary of the design parameters for the fan. The fan was a scale model designed and previously tested by GEAE, who designated the fan as "R4".

The fan was tested with a 0.20" blade tip clearance at the design point (100% corrected fan speed, or 12,657 RPMc). This clearance was selected as representative of a turbofan engine with many take-off and landing cycles.

In addition, this tip clearance minimized the chance of a fan rub event during testing. As part of the fan module design there were three distinct OGV designs, but they are not relevant for the purpose of this thesis, as discuss in the introduction of this section.



Figure 2.6: Fan module in the acoustic testing configuration installed on the UHB Drive Rig in the NASA Glenn 9- by 15-Foot Low Speed Wind Tunnel.

To establish the fan and OGV performance, the fan module installation included a uniform-inflow bell mouth inlet and either the fixed-area flight-type nozzle or a Variable area Fan Exit Nozzle (VFEN). The fixed area nozzle was used to obtain the fan performance on a representative operating line for a turbofan engine installation, at sea level conditions. The VFEN was used to obtain fan and stage performance across a range of fan speed operating conditions and simulated aircraft flight conditions. It consisted of a series of trapezoidal-shaped plates, each with a central radial pivot, arranged circumferentially in an annular duct. The plates moved in pairs in opposing directions to one another, like double doors. The fan operating point was changed by varying the exit area, and therefore the back pressure on the fan, while at a constant fan speed.

No. of Fan Blades	22
Fan Tip Diameter	22 in
Radius Ratio	0.30
Corrected Tip Speed	1,215 ft/sec
Corrected RPM	12,657
Corrected Fan Weight Flow	100.5 lbm/sec
Specific Flow	41.8 lbm/sec-ft ²
Stage Pressure Ratio	1.47
Design Bypass Ratio	8.85

Table 2.1: Fan design parameters (from [8])

Instrumentation

Freestream conditions in the wind tunnel were determined using a ceiling mounted pitot-static rake with thermocouples located near the entrance to the test section. Total pressure and total temperature conditions directly upstream of the fan were measured with this rake. Within the fan module, the fan weight flow was determined from static pressure measurements obtained within the bell mouth inlet and a flow correlation function relating the average of the bell mouth static pressures and the fan weight flow.

Fan and stage performance were determined using fixed total pressure/total temperature rakes mounted behind the fan and OGVs. Fan performance was obtained using three rakes and stage performance was obtained with seven rakes. Each rake consisted of seven measurement sensors, and each sensor contained a total pressure probe and a total temperature probe co-located within an aspirated stagnation tube. The sensors on each rake were located

radially in such a way as to provide flow conditions at the centre of equal areas. In addition, surface mounted static pressures were located at several axial locations in the fan module for calculating internal velocities.

Test procedure

The fan and OGV, or stage, aerodynamic performance was obtained for the fan and in combination with each OGV configuration. A Mach number of 0.05 was set in the test section during testing in order to provide uniform temperature and pressure distributions into the fan, and to prevent the fan from creating and ingesting vortices from the test section surfaces.

Fan and Stage Mapping Fan and stage performance mapping were conducted with the bell mouth inlet and the VFEN installed on the fan module. A performance map is a plot of the measured fan or stage performance parameter (total pressure ratio, total temperature ratio, or adiabatic efficiency) as a function of the corrected fan weight flow for a series of constant fan speed lines along which the fan weight flow is varied from minimum (toward a fan stall condition) to maximum (toward the aircraft high velocity/high altitude cruise condition) with the VFEN. The fan stall condition was avoided in order to minimize the risk of potentially damaging the fan blades if a rapid hard stall was encountered that produced a fan rub, even though the fan rub strip was designed for fan tip incursions. Therefore, the minimum fan weight flow was achieved when the fan blade stress measured with blade mounted strain gauges reached a predetermined limit. This limit varied with fan speed. The maximum weight flow was achieved at the maximum nozzle area with the VFEN fully open. Corrected fan speeds from 50% to 100% of corrected fan design speed were set, corresponding to corrected fan speeds from 6,328 to 12,657 RPMc. For the stage adiabatic efficiency, the assumption was made that there is no loss in total temperature loss across the OGVs and therefore the total temperature data from the fan performance rakes were used in the calculations. In order to more directly compare the stage performance between OGV configurations, a stage performance loss coefficient for total pressure was defined.

Fixed Nozzles Operating Line Fan performance on the operating line represented by the fixed area nozzle near sea level conditions was obtained using the bell mouth inlet and fixed area, flight-type, nozzle. Corrected fan design speeds from 40 to 100.7%, corresponding to 5,063 to 12,746 RPMc, were set. This fan speed range represented engine power settings from ground idle to full power take-off. With the fixed area nozzle installed, only the

fan performance was obtained since the stage performance rakes could only be installed with the VFEN testing configuration. However, once the fan weight flow and fan operating parameters were established for the fixed nozzle operating line, the corresponding stage performance was obtained with the VFEN installed by adjusting the nozzle exit area to match the fixed nozzle fan performance at the corresponding fan operating conditions.

Results and Discussion

Fan Performance Maps The fan total pressure ratio, total temperature ratio and adiabatic efficiency performance maps are presented in Figures 2.7a through 2.7c.

The fan results with this OGV configuration were selected because they are the most complete in terms of fan operating range. For reference, the fixed nozzle operating line results obtained during testing at sea level conditions are shown as the solid line that crosses the fan speed lines. The fan performance at the three operating conditions used for engine noise certification known as the acoustic rating points, representative of the aircraft flight operating points at approach, cutback, and take-off (61.7, 87.5, and 100% corrected fan speed), for this fan design are shown as solid symbols on the fixed nozzle operating line in all the figures.

Figure 2.7a shows the total pressure ratio fan map and Figure 2.7b shows the total temperature ratio fan map. In both figures, the minimum fan weight flow operating point on each fan speed line appears close to the fixed nozzle operating line, which would seem to indicate that the fan stall line is close to the fixed nozzle operating line. However, as discussed earlier, the minimum fan weight flow condition on each fan speed line represents a fan blade stress limit to prevent fan stall, and the fan stall line would be located further to the left in both figures. The adiabatic efficiency fan map is shown in Figure 2.7c. The fixed nozzle operating line results are again shown as the solid line that intersects all the fan speed lines. In the figure, the fixed nozzle operating line does not appear very smooth over the fan weight flow operating range. As the fan speed increases, the results indicate a slight wiggle in the adiabatic efficiency at the higher weight flow conditions for speeds at 87.5% corrected fan speed and lower. The reason for this phenomenon is not clear but may be an indication of a flow transition or flow instability on the fan blade at those fan speeds and aerodynamic loading conditions. The adiabatic efficiency begins to exhibit a peak in the performance level beginning at the 87.5% corrected fan speed line. The performance peaks at the highest fan speed lines are sharp, indicating the sensitivity of the fan blade to incidence angle at the higher weight flow conditions. The fan adiabatic

efficiency reaches the highest level of 0.926 or 92.6%, at 101.4 lbm/sec weight flow on the 100% corrected fan speed line, near the fan weight flow design point. For this type of high bypass fan design, the peak performance is on the low side. On the fixed nozzle operating line at sea level conditions, the results show that the adiabatic efficiency is down significantly from the peak levels at all fan speed lines, from 1.4% at higher fan speeds to 3.4% at lower fan speeds, indicating that the fan operates fairly far off from the optimum fan performance (this was a pre-existing fan, designed to be used with a core simulator, and therefore the level of fan performance was deemed to be acceptable).

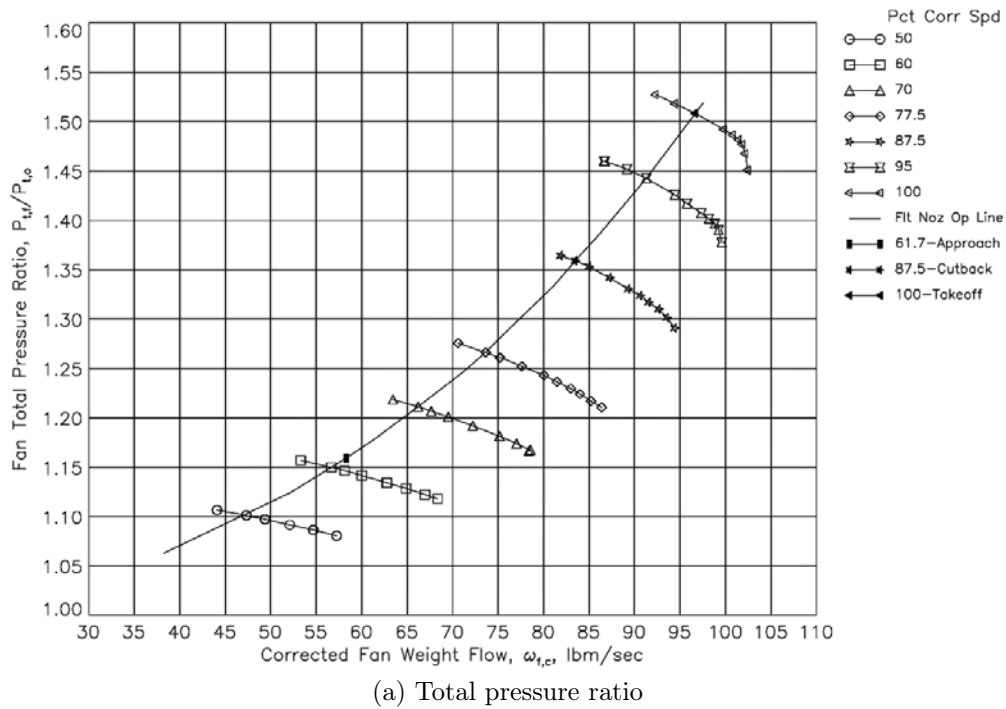
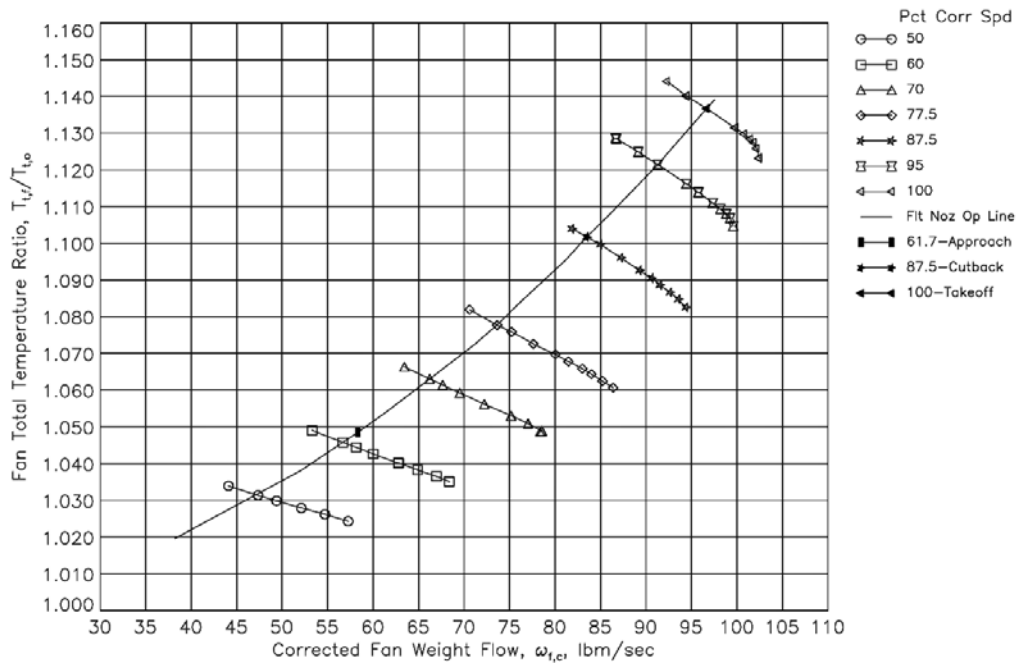
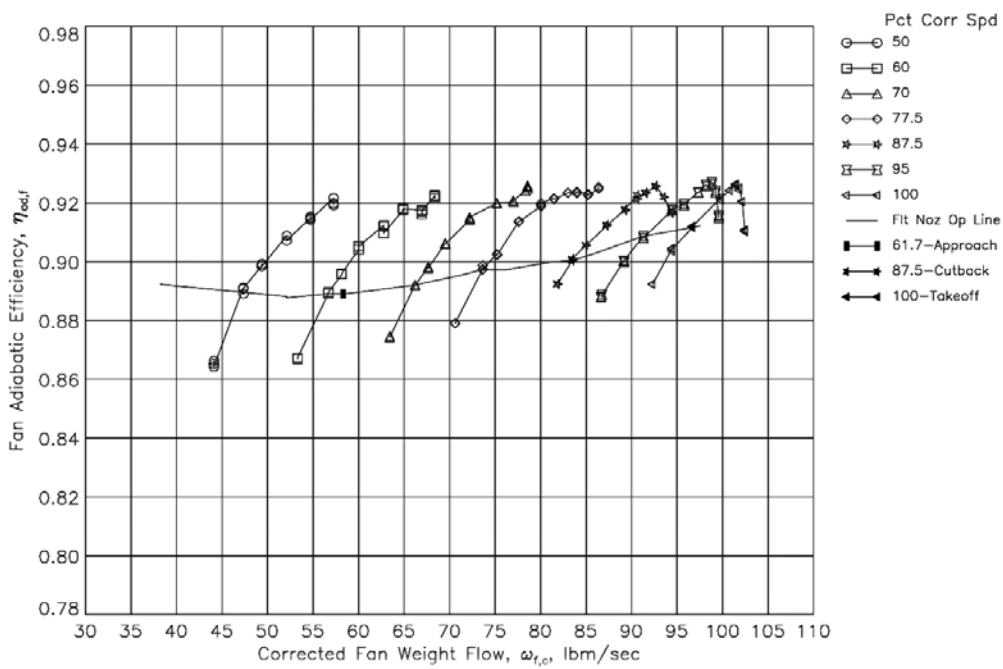


Figure 2.7: Fan performance maps with the Low Noise OGVs installed from [8] (continued).



(b) Total temperature ratio



(c) Adiabatic efficiency

Figure 2.7: Fan performance maps with the Low Noise OGVs installed from [8] (concluded).

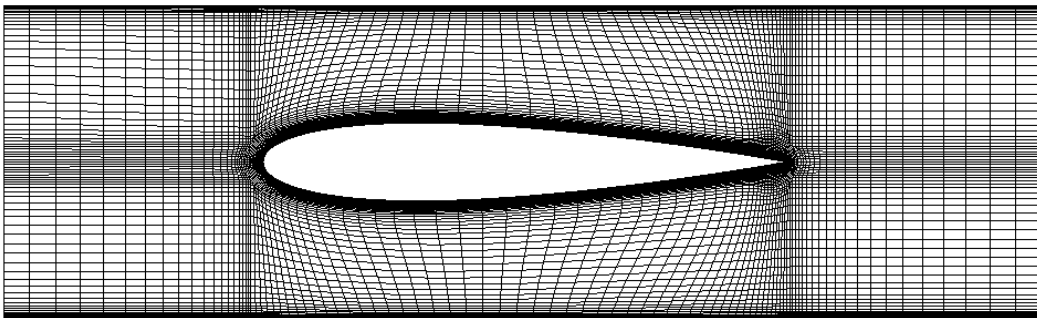
2.2.2 Metal blockage implementation

The present metal blockage implementation exclusively relies on source terms on the right-hand side of the RANS equations and its theoretical formulation was presented in a previous section. The values of the blockage factor b , as presented in equation (2.20), are directly computed from the blade geometry and then saved in a text file. At each cell center of the meridional mesh used in body force computations the corresponding blockage value, previously calculated, is assigned using cell coordinates. The blockage derivatives are computed within the CFD solver using a second order reconstruction technique.

Test case blockage

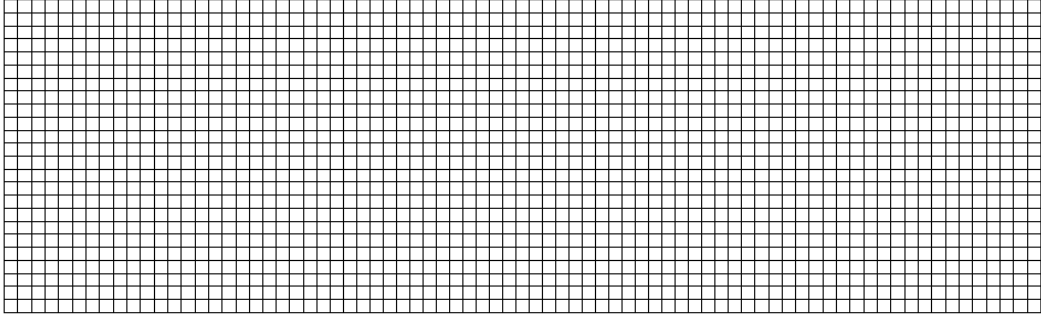
To check the implementation of the metal blockage source terms, 2D Euler computations are conducted on a NACA 0015 profile within a channel and with an axial inflow. The stagnation state is defined at the domain inlet, specifying stagnation temperature and stagnation pressure values, while a uniform static pressure is imposed at the outlet of the channel. Wall boundaries are used on the lower and upper side of the domain. With this boundary conditions the mass flow rate is a result of computation.

Body force computations are performed on the same domain with the same boundary conditions, but blade geometry is replaced by source terms. The blockage source terms are only active in the corresponding area enclosed between the leading and trailing edges of the NACA profile. The two different mesh grids are illustrated in Figures 2.8a and 2.8b.



(a) NACA 0015 profile test case

Figure 2.8: Blockage test case mesh grids (continued).



(b) Blockage source terms test case

Figure 2.8: Blockage test case mesh grids (concluded).

The presence of the NACA profile creates a restricted passage section (throat section) within the channel. The domain is then comparable to a convergent-divergent nozzle and, based on the static pressure value imposed at the outlet, both subsonic and supersonic inviscid flow regimes are possible.

Using values reported in Table 2.2, especially the area ratio between inlet and throat sections, and the correlations for the isentropic flow present in literature [1], it is possible to estimate the Mach numbers and the static pressure values at the outlet of the domain for subsonic and supersonic outflow solutions without shock waves in the channel, as shown in Table 2.3.

Area throat [m^2]	0.45
Area inlet /Area throat (Inlet)	1.333
Area inlet /Area throat (Outlet)	1.333
Total pressure p_0 (Inlet) [Pa]	101325
Total temperature T_0 (Inlet) [K]	288.4
Total density ρ_0 (Inlet) [$kg \cdot m^{-3}$]	1.224
Specific air constant R [$J \cdot kg^{-1} \cdot K^{-1}$]	287.04
Specific heat ratio k	1.4

Table 2.2: Geometric and fluid variables (fluid is air considered as an ideal gas)

Thanks to equation (2.24), due to St.Venant-Wantzel [1], the specific choke mass flow rate can also be predicted.

$$\frac{\dot{m}}{A} = \sqrt{2 \frac{k}{k-1} p_0 \rho_0 \left[\left(\frac{p}{p_0} \right)^{2/k} - \left(\frac{p}{p_0} \right)^{\frac{k+1}{k}} \right]} \quad (2.24)$$

	Subsonic outflow	Supersonic outflow
M	0.504	1.695
p/p_0	0.841	0.204
p [Pa]	85178.3	20701.4
\dot{m}/A [$kg \cdot s^{-1} \cdot m^{-2}$]	180.73	180.73
\dot{m} [$kg \cdot s^{-1}$]	108.44	108.44

Table 2.3: Theoretical values at the outlet for isentropic outflow solutions

Several simulations for the two domains have been carried out varying the static pressure at the outlet between the limit values indicated in Table 2.3. The results, in terms of static pressures trends, are summarized in Figure (2.9). The results from the reference CFD computations are tangentially averaged and compared to the body force simulations, which directly provide axisymmetric flow fields. The pressure profiles are similar and the shock waves are predicted by metal blockage source terms. This result is confirmed by the Mach number contour analysis, as illustrated in Figures 2.10a and 2.10b, where the case with $p/p_0 = 0.77$ at the outlet is chosen as reference. At last the choke mass flow rates resulting from the computations are identical in both models to the theoretical value provided by isentropic equations, as shown in Table 2.4.

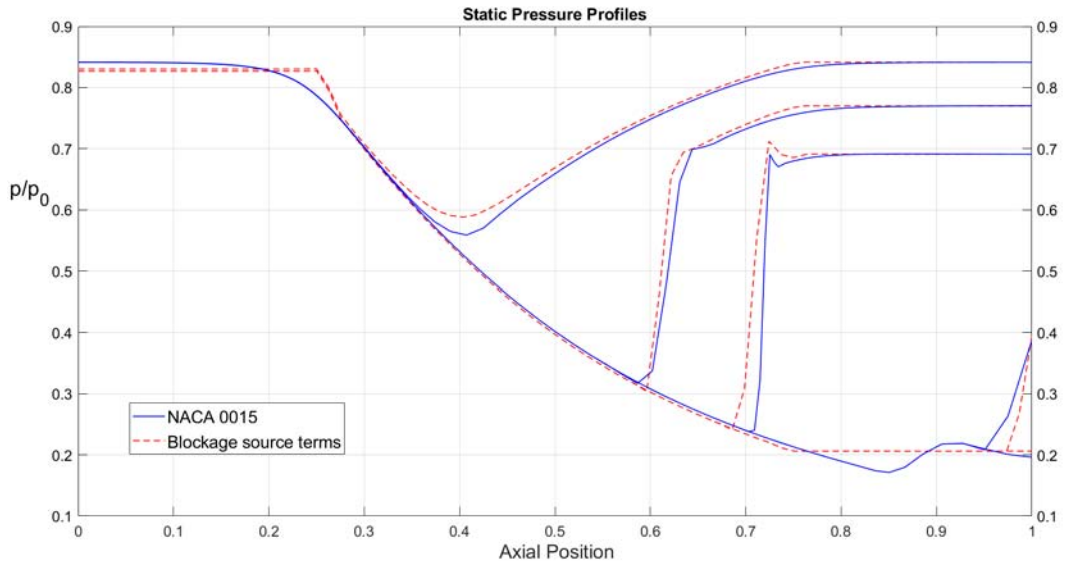
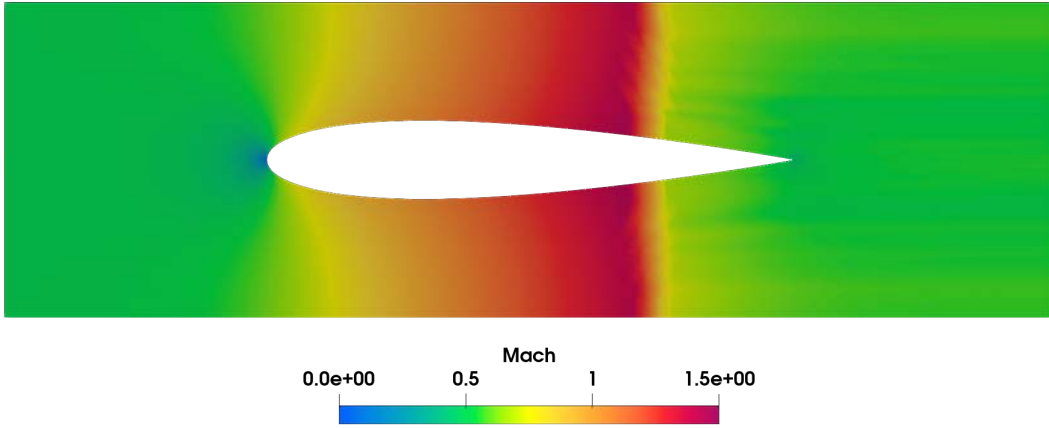
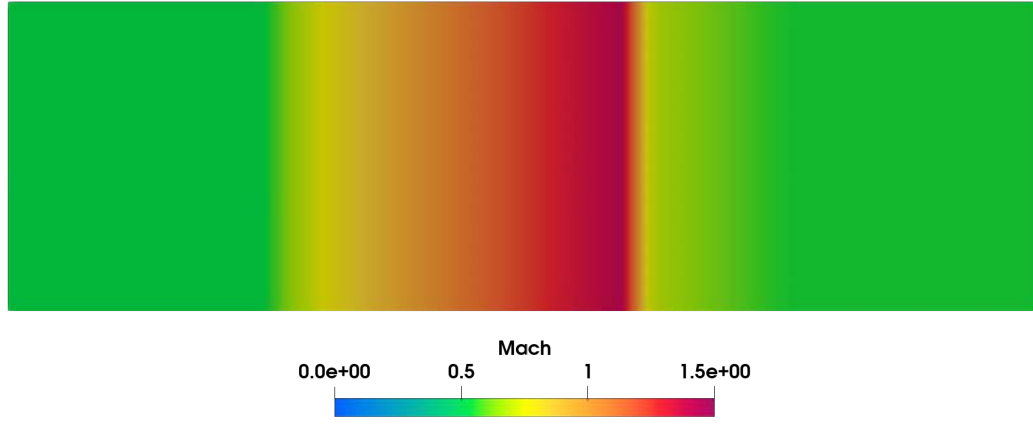


Figure 2.9: Axial pressure profiles within the domain for different static pressure values imposed at the outlet.



(a) NACA 0015 profile test case



(b) Blockage source terms test case

Figure 2.10: Mach number contours for simulations with a static pressure value of $p = 78000 \text{ Pa}$ imposed at the outlet.

$p \text{ [Pa]}$	NACA 0015			Blockage source terms		
	p/p_0	M	$\dot{m} \text{ [kg} \cdot \text{s}^{-1}]$	p/p_0	M	$\dot{m} \text{ [kg} \cdot \text{s}^{-1}]$
85250	0.841	0.503	108.35	0.841	0.501	108.04
78000	0.77	0.548	108.46	0.77	0.549	108.85
70000	0.691	0.606	108.43	0.691	0.607	108.71
40000	0.395	1.265	108.43	0.395	1.266	108.88
20888	0.206	1.680	108.43	0.206	1.688	108.88

Table 2.4: Numerical values computed at the outlet.

The results presented shows that the approach captures well metal blockage effects and it can be used effectively in other body force simulations. It is important to note that the addition of a source term to the density equation does not violate the conservative property of the solver. In the present case, the relative difference between the outlet and inlet mass flow rates was less than 0.05%.

2.2.3 Body force case

The assessment of the lift/drag body force model is done on the NASA/GE R4 fan stage as discussed before. The CFD solver used in this study is ANSYS Fluent and the case setting is described in this section.

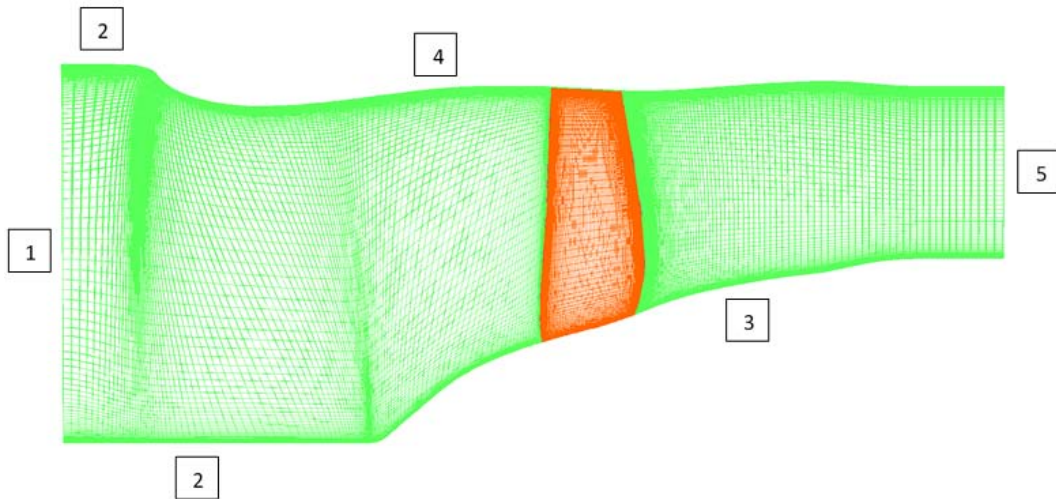


Figure 2.11: Mesh grid used in body force simulations

CFD computations of the fan are performed on a 3.6 million cells mesh shown in Figure 2.11. It is a 3D mesh obtained by revolution of the blade meridian plane around the rotation axis of 1 degree. In Figure 2.11 blade domain, the volume swept by blades in which body force source terms are active, is depicted in red. Boundary conditions are also enumerate in Figure 2.11 and they are defined as follow:

1. INLET: It is a pressure inlet where the total state and static pressure are imposed
 - $p_0 = 101325 \text{ Pa}$
 - $p = 80000 \text{ Pa}$

- $T_0 = 288.4 \text{ K}$
2. FLUID: Two fluid zones which are considered as stationary walls with a specified shear condition.
 3. HUB : It is a moving wall with a rotational speed of $\Omega = -1325.4379 \text{ m/s}$
 4. SHROUD: It is a stationary wall with a no slip shear condition.
 5. OUTLET: It is a pressure outlet where the total temperature and the static pressure are imposed
 - p is a value between 85000 Pa and 115000 Pa
 - $T_0 = 288.4 \text{ K}$

With these boundary conditions the mass flow rate is a result of the computation. Several simulations have been carried out using a density-based steady method with the one-equation turbulence model of Spalart-Allmaras. In each simulation a different static pressure value is imposed at the outlet (see chapter 3).

In order to compute the source terms described in previous sections, a dataset containing geometric informations on the real blade cascade is required. These data have been acquired using a 3D CAD program and saved in a text file. Then the file is loaded in ANSYS Fluent by a custom procedure described in next section.

2.2.4 CFD solver and body force module

The CFD solver used in this study is ANSYS Fluent. In order to apply the body force approach and the source terms introduced in previous sections, the program provides a specific utility, i.e. user-defined functions (UDFs). User-defined functions are C functions that allow to customize ANSYS Fluent and can significantly enhance its capabilities. A short description of the main UDFs and their usage is proposed below.

User-defined functions (UDFs)

A user-defined function, in according with [3], is a C function (written on a .c file extension, called "source file") that can be dynamically loaded with the ANSYS Fluent solver to enhance its standard features. For example, a UDF can be used to:

- Customize boundary conditions, material property definitions, surface and volume reaction rates, source terms in ANSYS Fluent transport equations, source terms in user-defined scalar (UDS) transport equations, diffusivity functions, and so on.
- Adjust computed values on a once-per-iteration basis.
- Initialize of a solution.
- Perform asynchronous (on demand) execution of a UDF.
- Execute at the end of an iteration, upon exit from ANSYS Fluent, or upon loading of a compiled UDF library.
- Enhance post processing.

UDFs are defined using ANSYS Fluent-supplied function declarations. These function declarations are implemented in the code as macros and are referred to as DEFINE (all capitals) macros. They are coded using additional macros and functions (also supplied by ANSYS Fluent) that access ANSYS Fluent solver data and perform other tasks. The definitions for DEFINE macros are contained in the udf.h header file, that must be included in the source file. One source file can contain a single UDF or multiple UDFs, and it is also possible to define multiple source files. Source code files containing UDFs can be either interpreted or compiled in ANSYS Fluent. After the UDF source files are interpreted or compiled, the function(s) contained in the interpreted code or shared library will appear in drop-down lists in dialog boxes, ready to be activated or "hooked" to the CFD model.

The most important DEFINE macros used in this study are the following:

DEFINE_ON_DEMAND It is a general-purpose macro that can be used to specify a UDF that is executed "on demand" in ANSYS Fluent, rather than having ANSYS Fluent call it automatically during the calculation. The UDF will be executed immediately, after it is activated, but it is not accessible while the solver is iterating.

DEFINE_INIT It is a general-purpose macro that can be used to specify a set of initial values for your solution. A DEFINE_INIT function is executed once per initialization and is called immediately after the default initialization is performed by the solver. Since it is called after the flow field is initialized, it is typically used to set initial values of flow quantities.

DEFINE_ADJUST It is a general-purpose macro that can be used to adjust or modify ANSYS Fluent variables that are not passed as arguments. For instance, DEFINE_ADJUST can be used to modify flow variables (for example, velocities, pressure) and compute integrals. A function that is defined using DEFINE_ADJUST executes at every iteration and is called at the beginning of every iteration before transport equations are solved.

DEFINE_SOURCE A DEFINE_SOURCE macro can be used to specify custom source terms for the different types of solved transport equations in ANSYS Fluent (except the discrete ordinates radiation model) including: mass, momentum, energy (also for solid zones), species mass fractions, P1 radiation model, user-defined scalar (UDS) transport, granular temperature (Eulerian, Mixture multiphase models).

Resolution scheme

The macros presented above have been successfully used to implement the Lift/Drag model within ANSYS Fluent. The steps followed by the solver for each simulation can be summarized as follow:

1. A DEFINE_ON_DEMAND is used to read from an external text file (previously prepared) the R4 geometric blade data and the calibration coefficients required by the body force source terms equations (2.9), (2.10), (2.11) and (2.5). Each value is assigned to the corresponding cell center within the blade domain and then stored into an array.
2. Once set the case (fluid properties, boundary conditions, turbulence model, solution process, etc.) the solver is ready to calculate the solution. The density-based procedure is adopted in this study and its schematic representation is illustrated in Figure 2.12.
3. The solution process for the density-based solver (Figure 2.12) begins with a two-step initialization sequence that is executed outside the solution iteration loop. This sequence begins by initializing equations to user-entered (or default) values taken from the ANSYS Fluent user interface. Next, PROFILE UDFs are called, followed by a call to INIT UDFs. Initialization UDFs overwrite initialization values that were previously set. A DEFINE_INIT is now used to initialize blockage and its gradient.

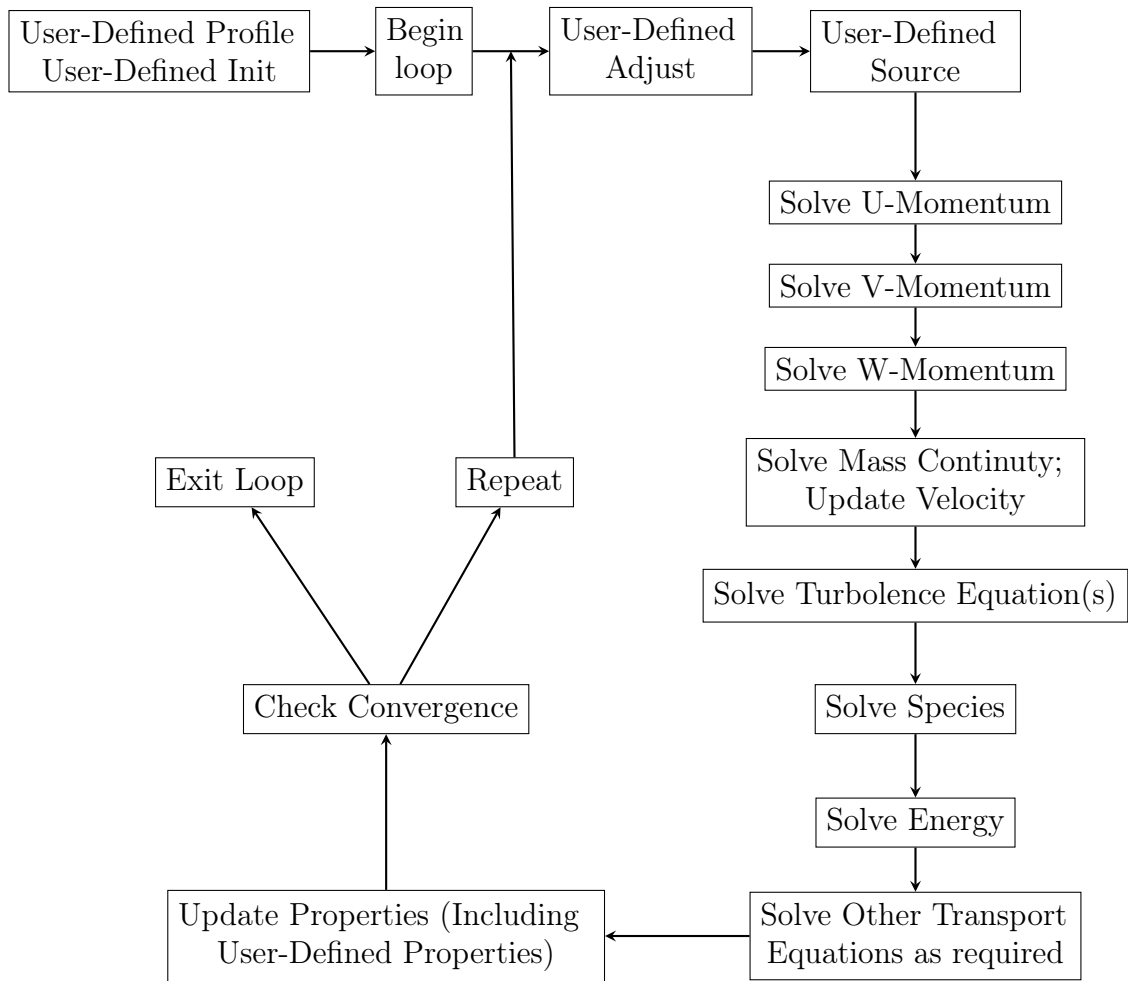


Figure 2.12: Solution procedure for density-based solver (from [3]).

4. The solution iteration loop begins with the execution of ADJUST UDFs. A DEFINE_ADJUST is used to compute the force modules expressed by the equations (2.9) and (2.10). The force are also computed as vectors, using geometric and fluid angles, and decomposed along the axis.
5. User-defined source are now called by the solver. Several DEFINE_SOURCE macros are used to specify the different source terms present on the right side of governing equations (2.21), (2.22) and (2.23).
6. Momentum equations for u, v, and w velocities are solved sequentially, followed by mass continuity and velocity updates. Subsequently, the

energy and species equations are solved, followed by turbulence and other scalar transport equations, as required.

7. After the conservation equations, properties are updated, including PROPERTY UDFs. Thus, if your model involves the gas law, for example, the density will be updated at this time using the updated temperature (and pressure and/or species mass fractions).
8. A check for either convergence or additional requested iterations is done, and the loop either continues or stops.

Chapter 3

Results and Discussion

A result comparison between the body force model implemented in this thesis and the R4 case (with discrete blades) is presented and discussed in this chapter. It is thought that the model must be able to reproduce the performance of an isolated fan stage for varying operating conditions to accurately capture fan-airframe interactions in an installed configuration.

To avoid confusion, the computations with the blade geometry are denoted as blade computations, as opposed to body force computations.

3.1 Fan performance maps

Several blade and body force computations have been carried out using the boundary conditions described in section 2.2.3.

In Table 3.1 the static pressure values imposed at the outlet for different simulations are listed along with computations results. The rotational speed was set constant at maximum design value (RPM 100%), thus the results computations allowed to reconstruct an operating speed line.

The fan total pressure ratio (TPR), total temperature ratio (TTR) and adiabatic efficiency (η_{is}) performance maps are presented in Figures 3.1a through 3.1c. These three quantities are computed using the following equations

$$TPR = \frac{p^0}{p_{inlet}^0} \quad (3.1)$$

$$TTR = \frac{T^0}{T_{inlet}^0} \quad (3.2)$$

$$\eta_{is} = \frac{TPR^{\frac{k-1}{k}} - 1}{TTR - 1} \quad (3.3)$$

where p^0 and T^0 are respectively the mass-flow averaged total pressure and total temperature computed one-chord downstream the blade trailing edge location.

The speed lines from blade computations are depicted in blue, while red and green speed lines represent body force computations for the base-model and the calibrated-model respectively. The calibration coefficient C was calculated using the equation (2.14), where the value assigned to the constant C_0 is

$$C_0 = 0.0375 \quad (3.4)$$

within the range $[0.01, 0.05]$ suggested by Thollet [13].

Comparing the performance maps in Figures 3.1a through 3.1c with the experimental data of the Source Diagnostic Test (at 100% of corrected speed), illustrated in Figures 2.7a, 2.7b and 2.7c, it appears that the speed lines trends and their maximum value are captured by the blade computations. Therefore, the blue speed lines in Figures 3.1a through 3.1c represent a valid comparison for the body force computations.

In all performance maps body force computations (both for the basic and calibrated model) overestimate the mass flow rate compared to blade computations. However, the calibration process improves the mass flow rate predictions, especially regarding the choke mass flow rate: the error in estimating the maximum mass flow rate is 2.3% in the base body force model while just 0.4% in the calibrated model. It must be said the body force model implemented in this study correctly overestimate the mass flow rates. Since the blockage source terms used do not take into account the aerodynamic blockage (due to boundary layer presence on blade surfaces) the minimum passage section (throat section), within the blade-to-blade channel, is overestimated.

Focusing on Figures 3.1a and 3.1b it is clear that body force models do not overestimate just the mass flow rates but also the total pressure ratio and the total temperature ratio. Therefore, the work exchanged by the fan, expressed in equation (3.5), is increased.

$$Work = \frac{c_p T^0}{\eta_{is}} \left(TPR^{\frac{k-1}{k}} - 1 \right) \quad (3.5)$$

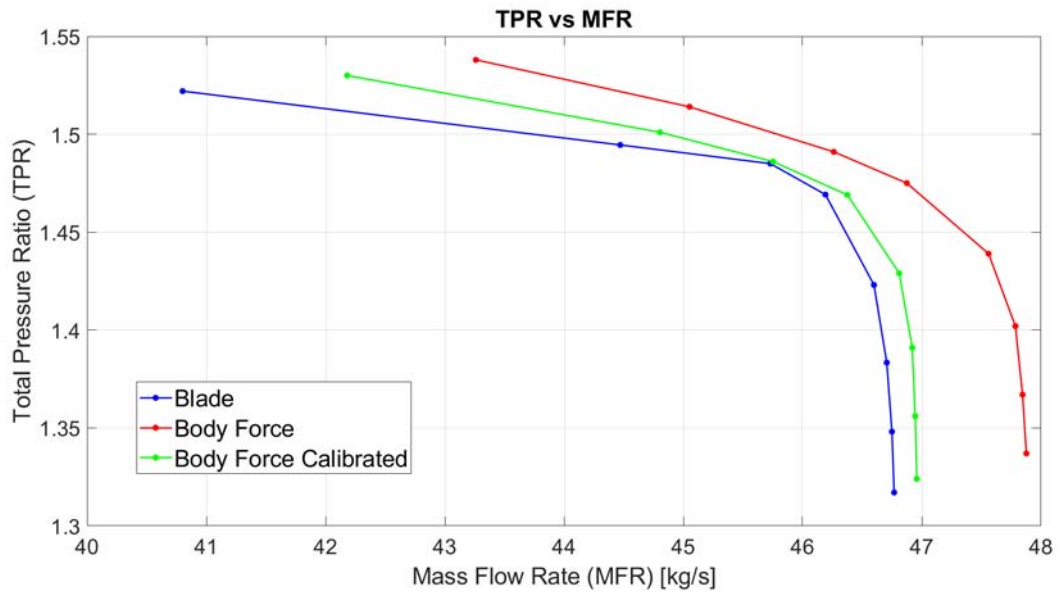
In according with Thollet, the calibration process reduces errors in work predictions.

However, the calibrated body force model presents a drawback. As shown in Figure 3.1c the maximum value of adiabatic efficiency is captured by the body force base-model, while it is underestimated by the calibrated model.

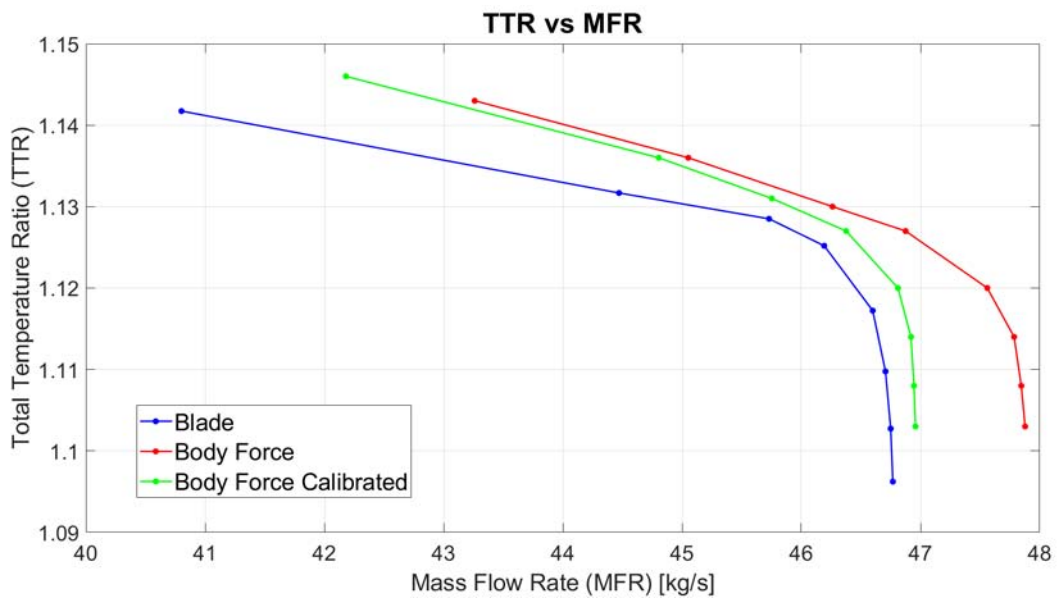
As discussed in section 2.1.3 the shape function C reduces the flow turning near the leading edge of the rotor thus the flow angle distribution in body force simulations differs from the one in the blade computation at maximum efficiency.

R4 blade model computations					
p [Pa]	Ω [m/s]	MFR [kg/s]	TPR	TTR	η_{is}
85000	1325.438	46.768	1.317	1.096	0.851
90000	1325.438	46.7498	1.348	1.103	0.867
95000	1325.438	46.706	1.383	1.101	0.885
100000	1325.438	46.599	1.423	1.117	0.905
105000	1325.438	46.192	1.469	1.125	0.928
107500	1325.438	45.7298	1.485	1.129	0.931
111000	1325.438	44.471	1.494	1.132	0.924
115000	1325.438	40.802	1.522	1.142	0.894
BF model computations results					
p [Pa]	Ω [m/s]	MFR [kg/s]	TPR	TTR	η_{is}
85000	1325.438	47.877	1.337	1.103	0.841
90000	1325.438	47.845	1.367	1.108	0.863
95000	1325.438	47.785	1.402	1.114	0.889
100000	1325.438	47.560	1.439	1.120	0.913
105000	1325.438	46.875	1.475	1.127	0.928
107500	1325.438	46.262	1.491	1.130	0.929
111000	1325.438	45.052	1.514	1.136	0.925
115000	1325.438	43.261	1.538	1.143	0.915
BF calibrated model computations results					
p [Pa]	Ω [m/s]	MFR [kg/s]	TPR	TTR	η_{is}
85000	1325.438	46.958	1.324	1.103	0.814
90000	1325.438	46.945	1.356	1.108	0.840
95000	1325.438	46.920	1.391	1.114	0.867
100000	1325.438	46.811	1.429	1.120	0.895
105000	1325.438	46.376	1.469	1.127	0.913
107500	1325.438	45.753	1.486	1.131	0.915
111000	1325.438	44.804	1.501	1.136	0.908
115000	1325.438	42.181	1.530	1.146	0.886

Table 3.1: Mass-flow averaged results for different outlet pressure values computed one-chord downstream blade trailing edge location.

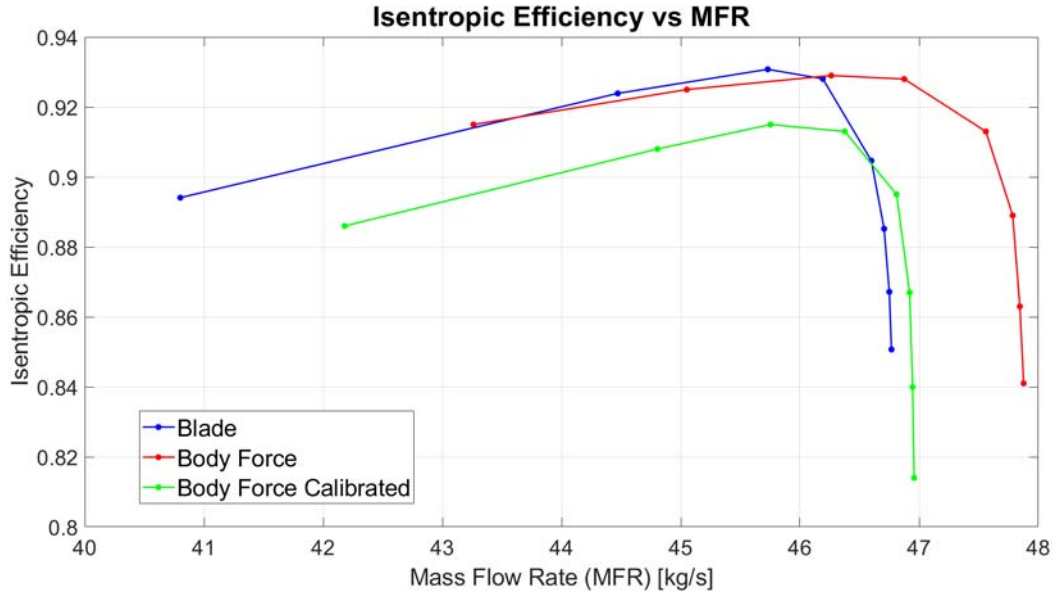


(a) Total pressure ratio performance map



(b) Total temperature ratio performance map

Figure 3.1: Fan performance maps (continued).



(c) Adiabatic efficiency performance map

Figure 3.1: Fan performance maps (concluded).

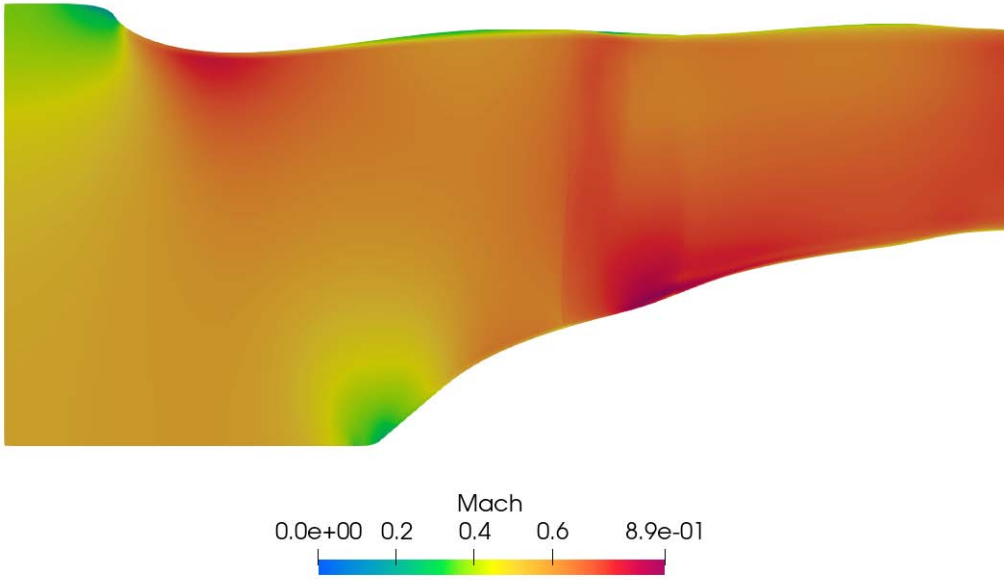
3.2 Contour analysis

In the previous section speed lines analysis showed that the body force calibrated model is more accurate than the non-calibrated model regarding the work and mass flow rate predictions, although it underestimates the adiabatic efficiency. In the present section this observation is confirmed by contour analysis of the following fluid quantities:

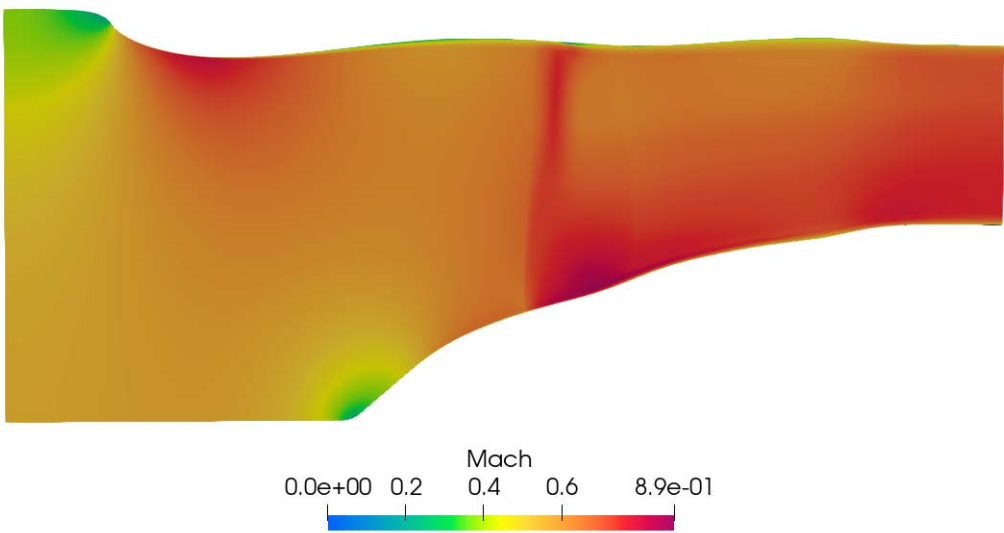
- Mach number M
- Specific mass flow rate ρu_z
- Total pressure ratio TPR
- Total temperature ratio TTR

For each quantity the calibrated model computation contours are compared with the blade computation contours. The computations at maximum mass flow rate and at peak efficiency are considered as reference. In these computations the imposed outlet pressures are $p = 85000 Pa$ and $p = 105000 Pa$ respectively.

3.2.1 Mach number ($p_{outlet} = 105000 Pa$)



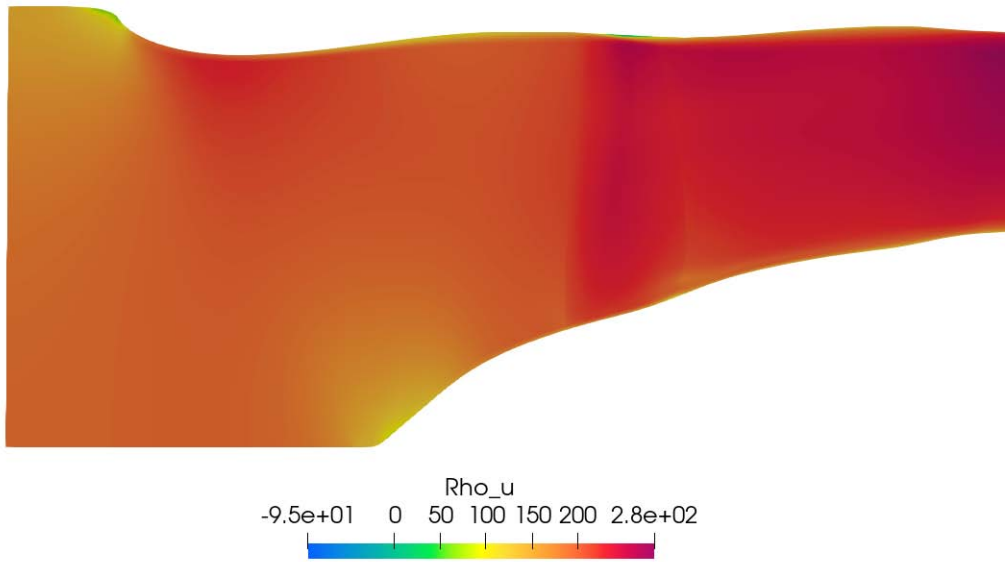
(a) Mach number contour for blade computation



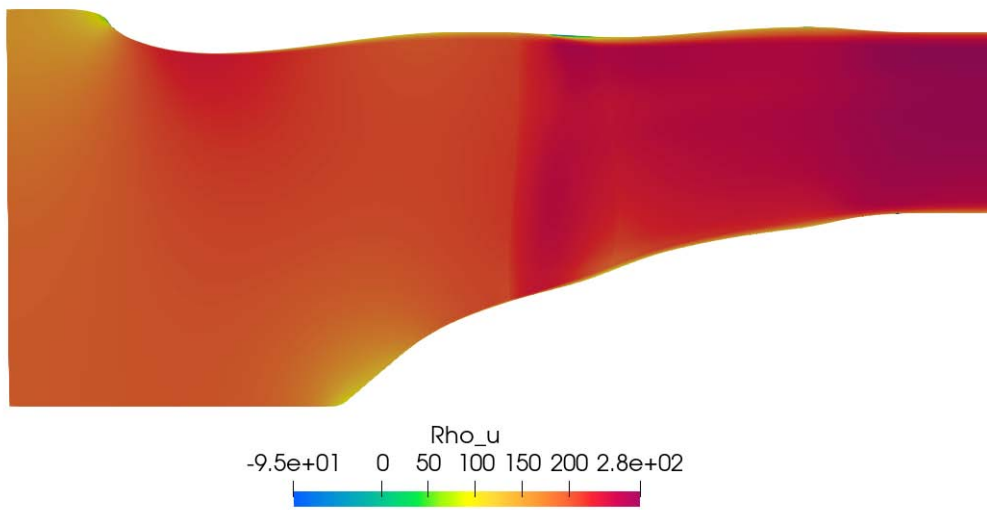
(b) Mach number contour for body force calibrated model computation

Figure 3.2: Mach number contours for computations with $p = 105000 Pa$ imposed at the outlet.

3.2.2 Specific mass flow rate ($p_{outlet} = 105000 Pa$)



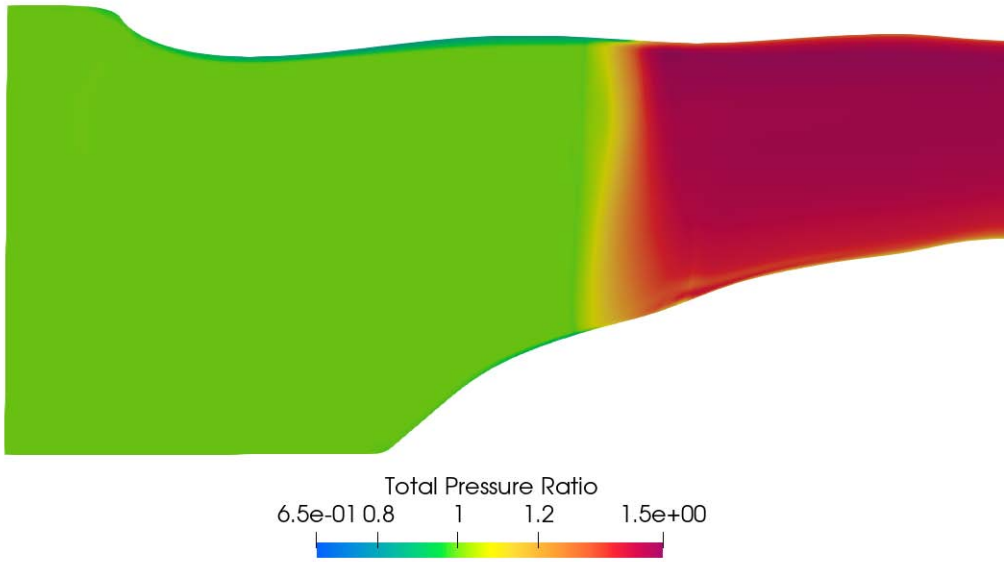
(a) ρu_z contour for blade computation



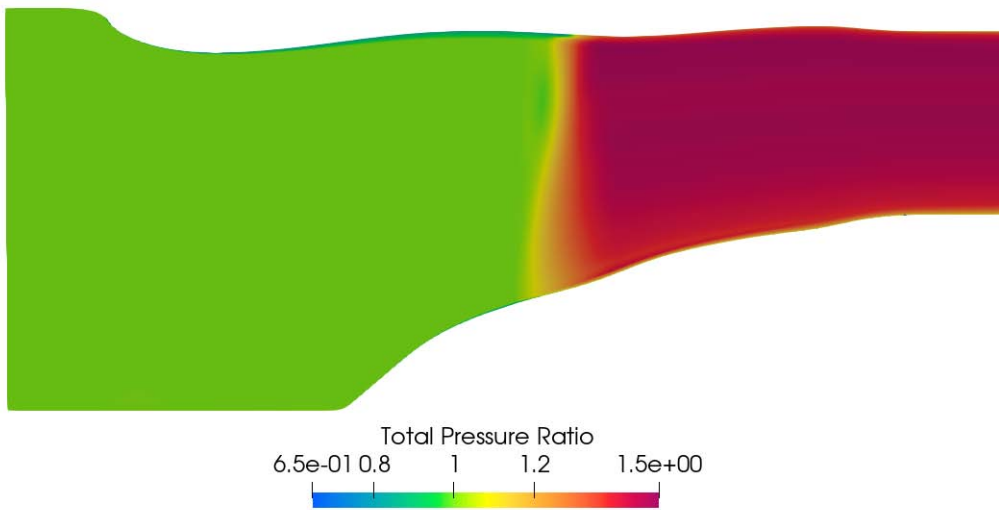
(b) ρu_z contour for body force calibrated model computation

Figure 3.3: Specific mass flow rate contours for computations with $p = 105000 Pa$ imposed at the outlet.

3.2.3 Total pressure ratio ($p_{outlet} = 105000 Pa$)



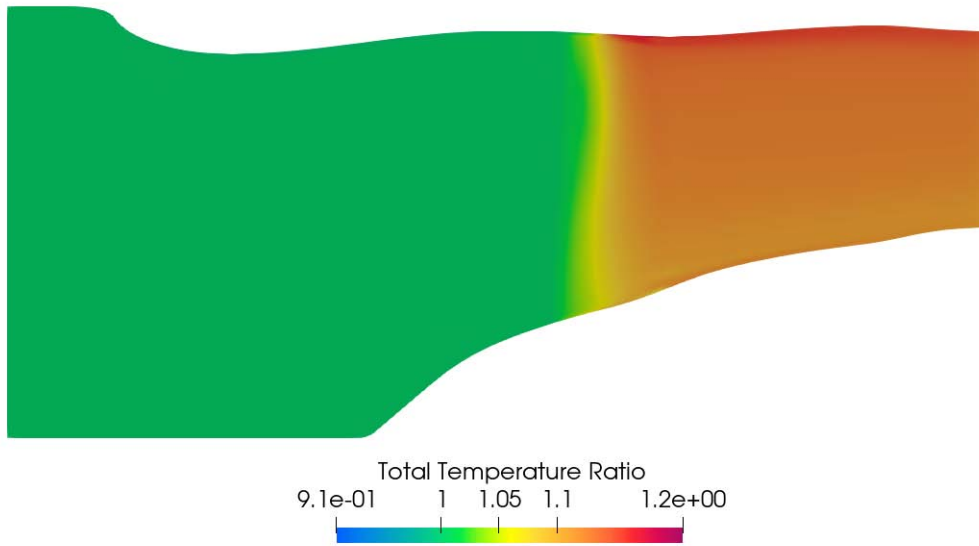
(a) *TPR* contour for blade computation



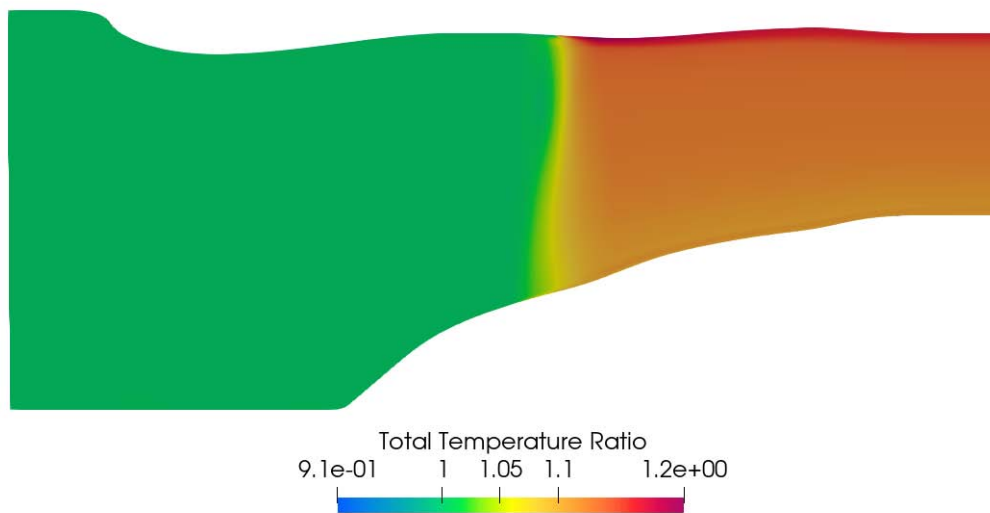
(b) *TPR* contour for body force calibrated model computation

Figure 3.4: Total pressure ratio contours for computations with $p = 105000 Pa$ imposed at the outlet.

3.2.4 Total temperature ratio ($p_{outlet} = 105000 Pa$)



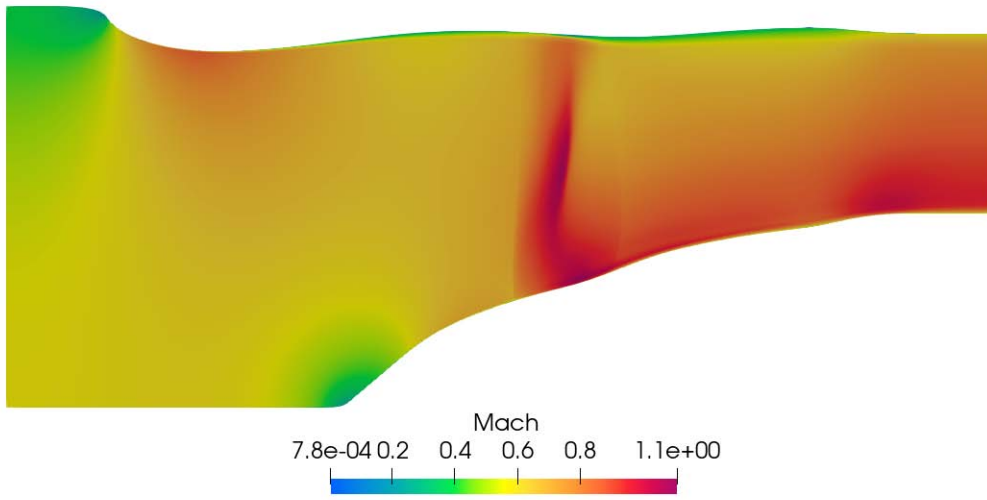
(a) *TTR* contour for blade computation



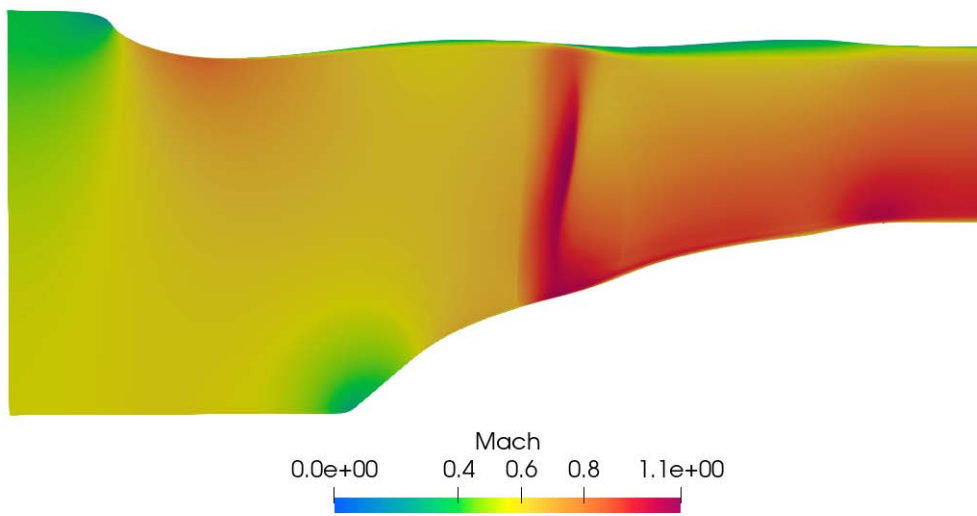
(b) *TTR* contour for body force calibrated model computation

Figure 3.5: Total temperature ratio contours for computations with $p = 105000 Pa$ imposed at the outlet.

3.2.5 Mach number ($p_{outlet} = 85000 Pa$)



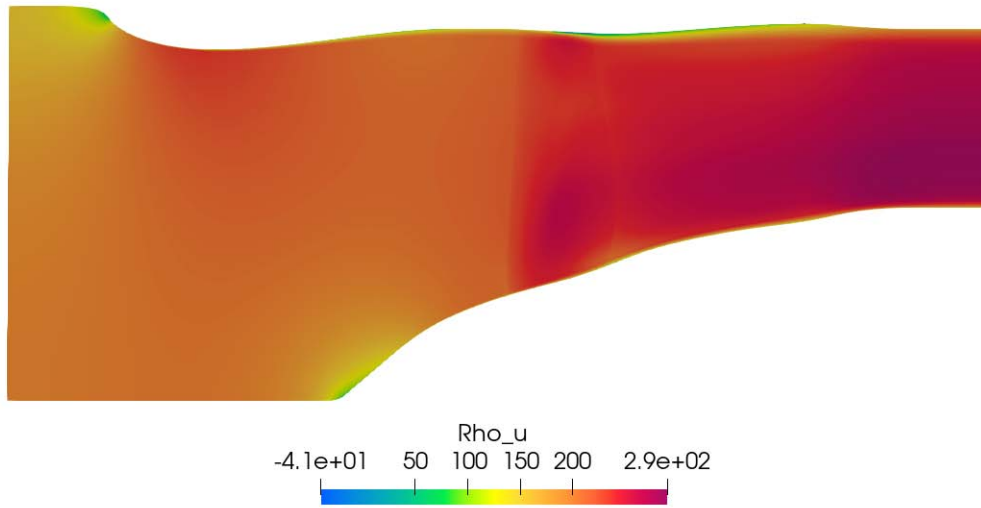
(a) Mach number contour for blade computation



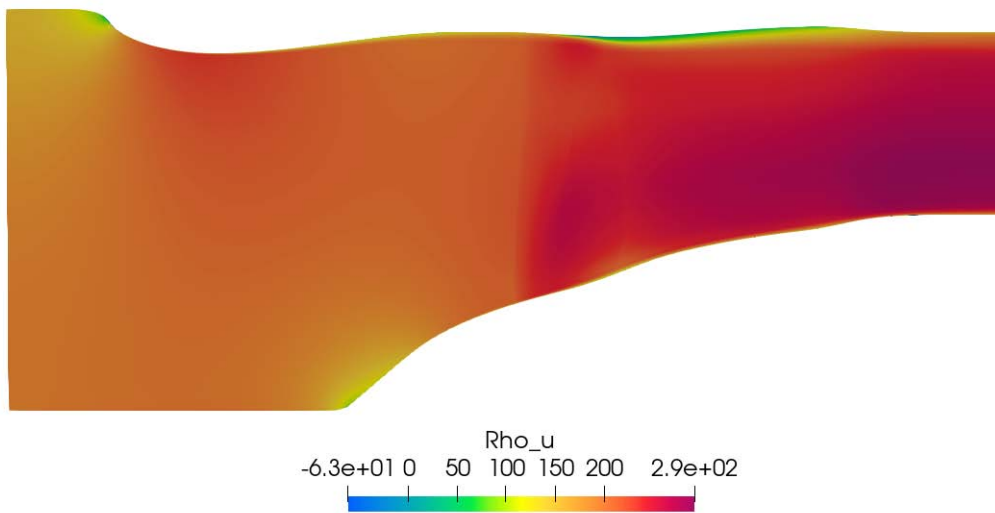
(b) Mach number contour for body force calibrated model computation

Figure 3.6: Mach number contours for computations with $p = 85000 Pa$ imposed at the outlet.

3.2.6 Specific mass flow rate ($p_{outlet} = 85000 Pa$)



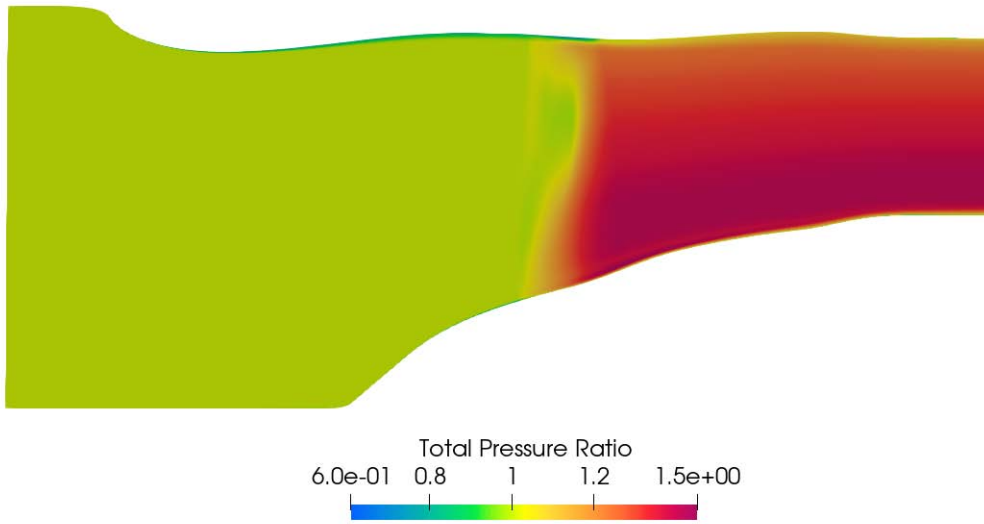
(a) ρu_z contour for blade computation



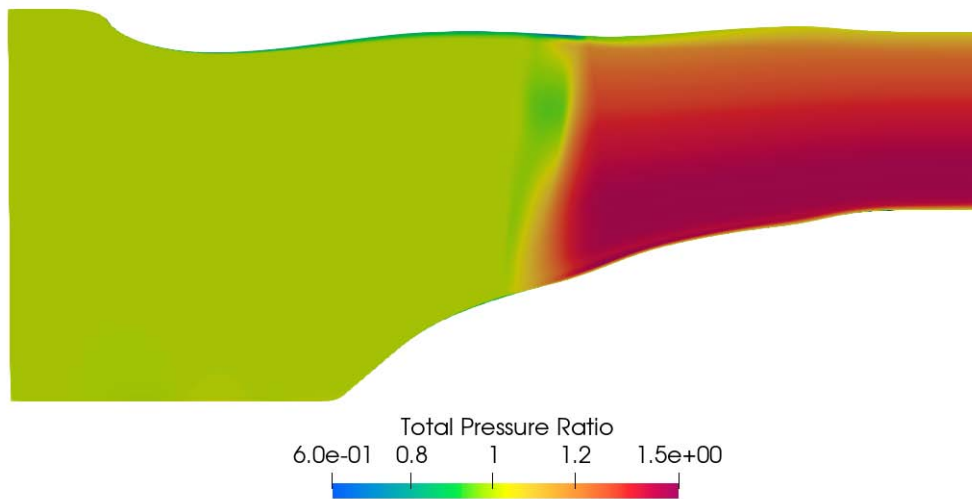
(b) ρu_z contour for body force calibrated model computation

Figure 3.7: Specific mass flow rate contours for computations with $p = 85000 Pa$ imposed at the outlet.

3.2.7 Total pressure ratio ($p_{outlet} = 85000 Pa$)



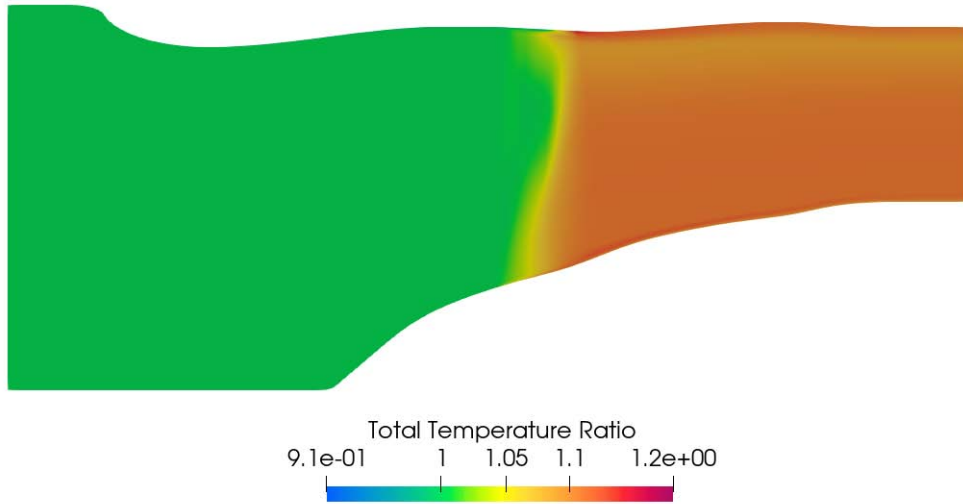
(a) *TPR* contour for blade computation



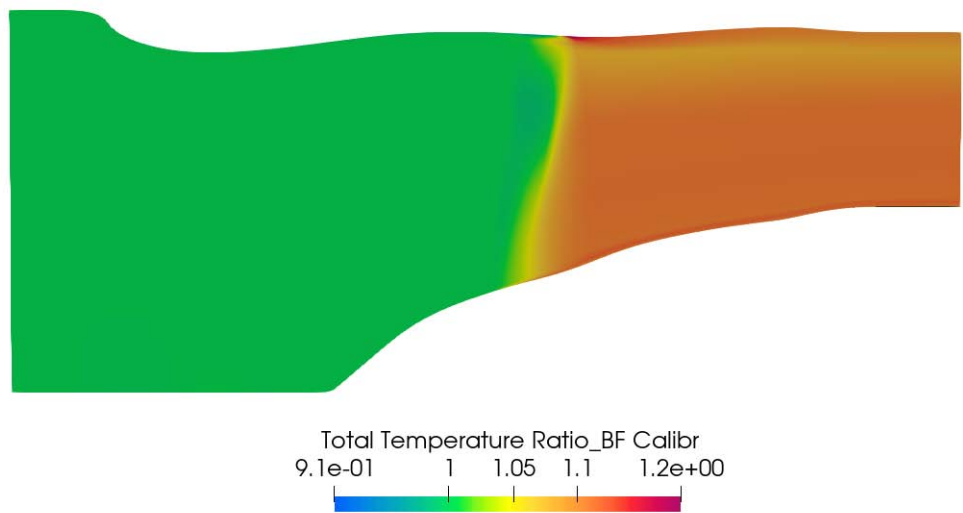
(b) *TPR* contour for body force calibrated model computation

Figure 3.8: Total pressure ratio contours for computations with $p = 85000 Pa$ imposed at the outlet.

3.2.8 Total temperature ratio ($p_{outlet} = 85000 Pa$)



(a) *TTR* contour for blade computation



(b) *TTR* contour for body force calibrated model computation

Figure 3.9: Total temperature ratio contours for computations with $p = 85000 Pa$ imposed at the outlet.

3.3 Spanwise analysis

The contour analysis reveals a good correspondence between the fluid variables trends within the fan stage. This evidence is further confirmed by the spanwise trends of the following quantities:

- Specific mass flow rate ρu_z
- Adiabatic efficiency η_{is}
- Swirl angles α and β
- Pressure coefficient ψ and flow coefficient ϕ

where η_{is} is defined in equation (3.3), α and β , defined in equations (3.6) and (3.7), are the absolute and relative velocity angles respectively, ψ and ϕ are defined in equations (3.8) and (3.9) (U_{tip} is the peripheral speed at blade tip)

$$\alpha = \text{atan}(V_\theta/V_z) \quad (3.6)$$

$$\beta = \text{atan}(W_\theta/W_z) \quad (3.7)$$

$$\psi = \frac{H^0 - H_{inlet}^0}{U_{tip}^2} \quad (3.8)$$

$$\phi = \frac{W_z}{U_{tip}} \quad (3.9)$$

Each quantity is defined using flow variables computed one-chord downstream the blade trailing edge location. As in the previous section the results from computations at maximum mass flow rate and at peak efficiency are chosen as reference.

Figures 3.10 and 3.14 show the specific mass flow rate trends for two cases. For $p_{out} = 105000 Pa$ basic and calibrated model present the same trends, which are also close to blade computation results. Near hub both models provide higher values of specific mass flow rate because axial velocities are higher, as proved by ψ trend in Figure 3.13. For span values higher than 3% calibrated results are slightly lower than basic model ones: the overall area, which stands for the integral value, is smaller and closer to blade computation result in the calibrated model (in according with results reported in Table 3.1). For $p_{out} = 85000 Pa$ there is again an analogy in body force models results between specific mass flow rate and ϕ trends. Near the hub all models provide similar results. For span values higher than 3% the basic and calibrated model results, which have a similar trend, overestimate

blade computation results at first, while they underestimate them near tip. Higher velocities are present in body force domain which lead to an increased specific mass flow rate at middle span on the one hand and to a wider wake near the hub (then a lower specific mass flow rate) on the other. These changes in fluid velocity, depicted in Figure 3.6, are due to an overturning imposed by the source terms in the upper half of blade zone.

Figures 3.11 and 3.15 show the adiabatic efficiency trends for two cases. The basic model almost captures the global efficiency while the calibrated model underestimates it, as reported in Table 3.1. However, both model trends differ from blade computations results. For $p_{out} = 105000 Pa$ both body force models overestimate the efficiency near the hub: although the work coefficient predictions are lower than blade results, as shown in Figure 3.13, the losses are reduced. For span values higher than 0.5 the basic model captures blade computation results while the calibrated model underestimates them. This is due to the calibration process: distorted flow angle distribution introduces losses within blade zone, which reduce the total pressure ratio. For $p_{out} = 85000 Pa$ the results are different. In the lower half of blade zone both body force model results match or overestimate blade results, while near tip these two models underestimate the efficiency. This is due to an incorrect flow angle distribution in both models, which provides total temperature ratio reduction, as shown in Figure 3.8.

In Figures are depicted the flow angles and ψ - ϕ coefficients respectively. These quantities are mutually dependent. For $p_{out} = 105000 Pa$ body force ϕ values overestimate blade results, especially near hub. Body force ψ results present the following trend: for span values lower than 0.2 blade results are underestimated while they are overestimated near tip. This is due to flow angles trends: near hub there is an underturning while an overturning is provided at tip location. For $p_{out} = 105000 Pa$ body force ϕ and especially ψ trends differ from blade results. On the one hand this is due flow angles trends, as stated in previous case, but on the other to model inadequacy. A body force method reconstructs the average flow field, therefore rapid changes in fluid variables gradient cannot be captured. Furthermore, the calibration process is arbitrary and, as recognized by its author, it loses the correlation with blade results, partially restoring the match only at the level of integrated quantities.

3.3.1 Specific mass flow rate ($p_{outlet} = 105000 Pa$)

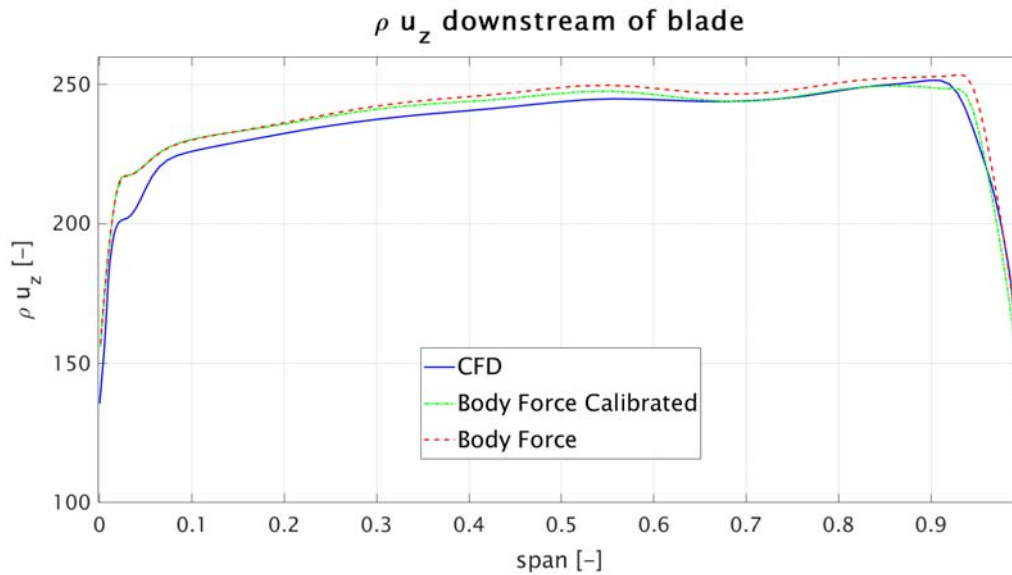


Figure 3.10: Specific mass flow rate ($p_{outlet} = 105000 Pa$)

3.3.2 Adiabatic efficiency ($p_{outlet} = 105000 Pa$)

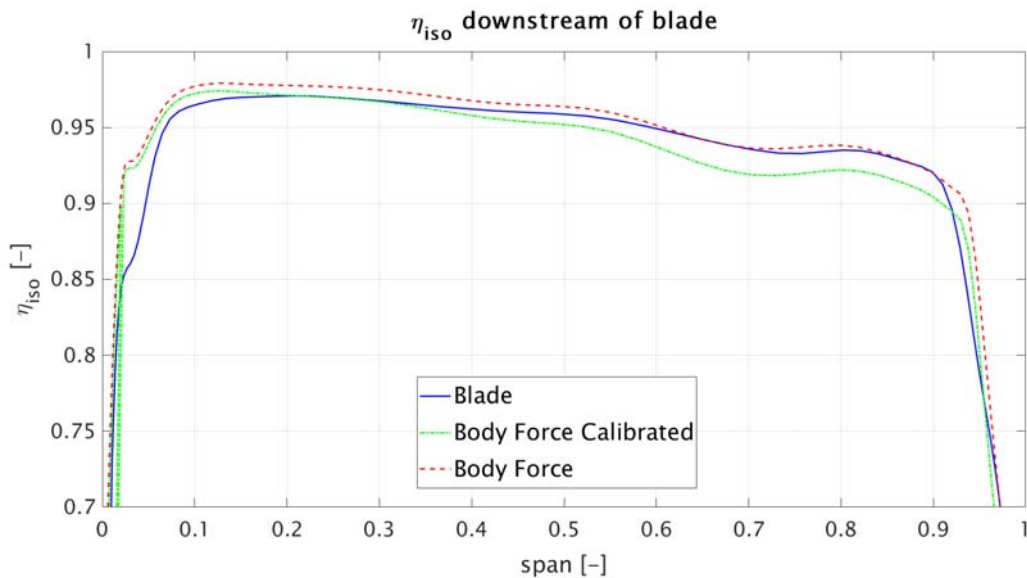


Figure 3.11: Adiabatic efficiency ($p_{outlet} = 105000 Pa$)

3.3.3 Swirl angles ($p_{outlet} = 105000 Pa$)

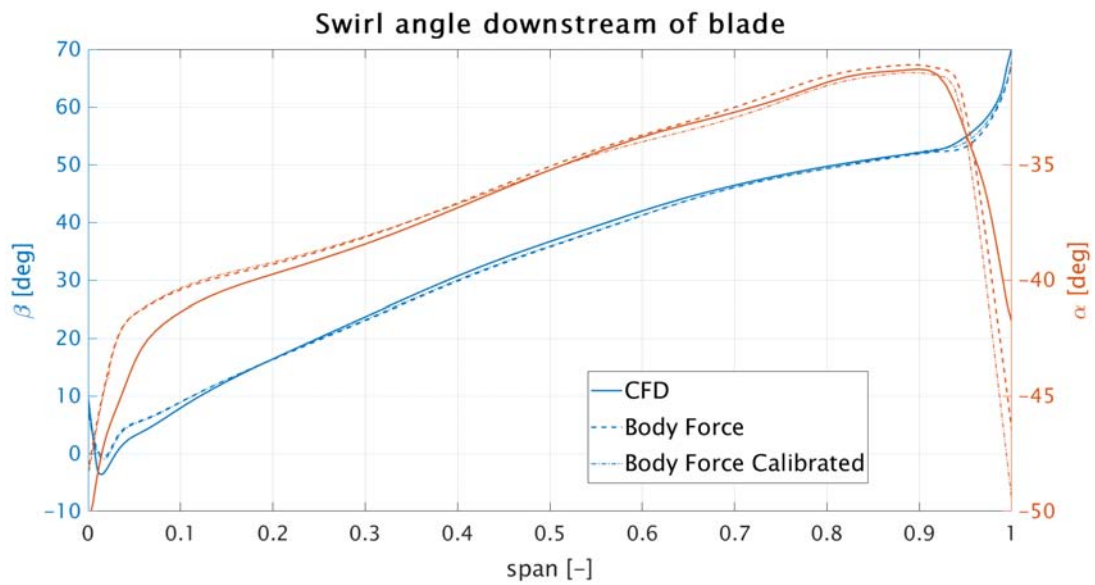


Figure 3.12: Swirl angles ($p_{outlet} = 105000 Pa$)

3.3.4 Pressure and Flow coefficients ($p_{outlet} = 105000 Pa$)

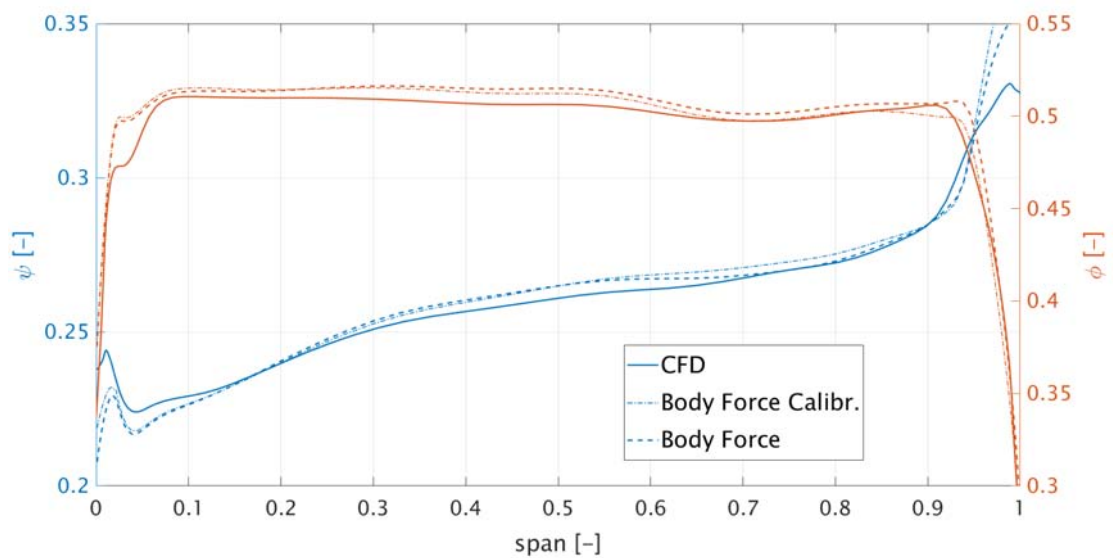


Figure 3.13: Pressure and Flow coefficients ($p_{outlet} = 105000 Pa$)

3.3.5 Specific mass flow rate ($p_{outlet} = 85000 Pa$)

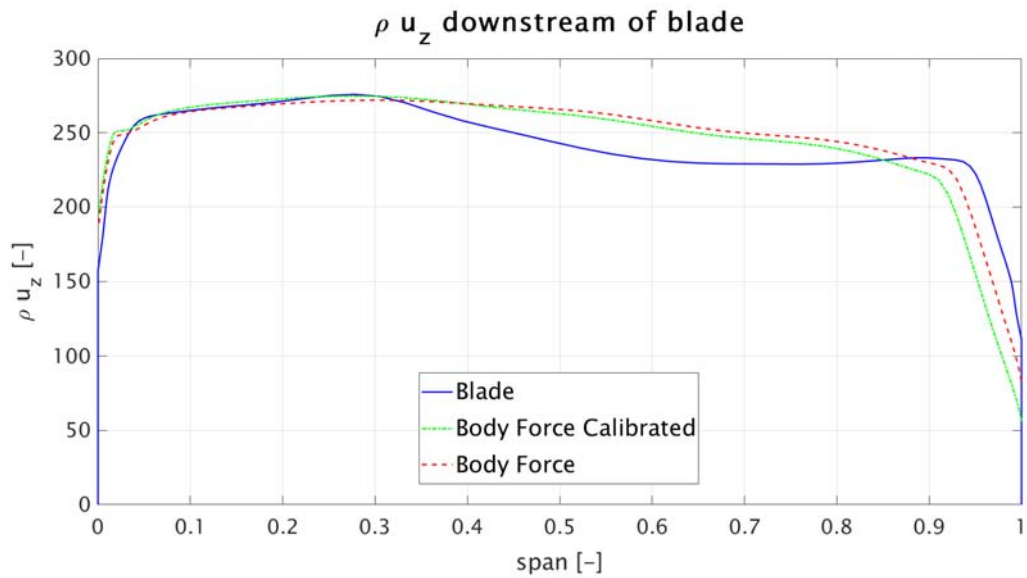


Figure 3.14: Specific mass flow rate ($p_{outlet} = 85000 Pa$)

3.3.6 Adiabatic efficiency ($p_{outlet} = 85000 Pa$)

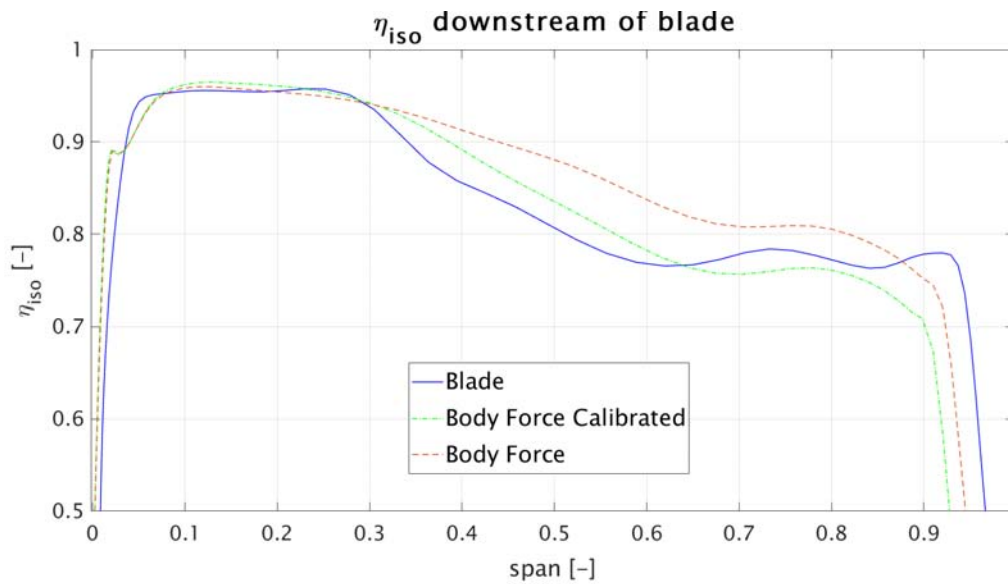


Figure 3.15: Adiabatic efficiency ($p_{outlet} = 85000 Pa$)

3.3.7 Swirl angles ($p_{outlet} = 85000 Pa$)

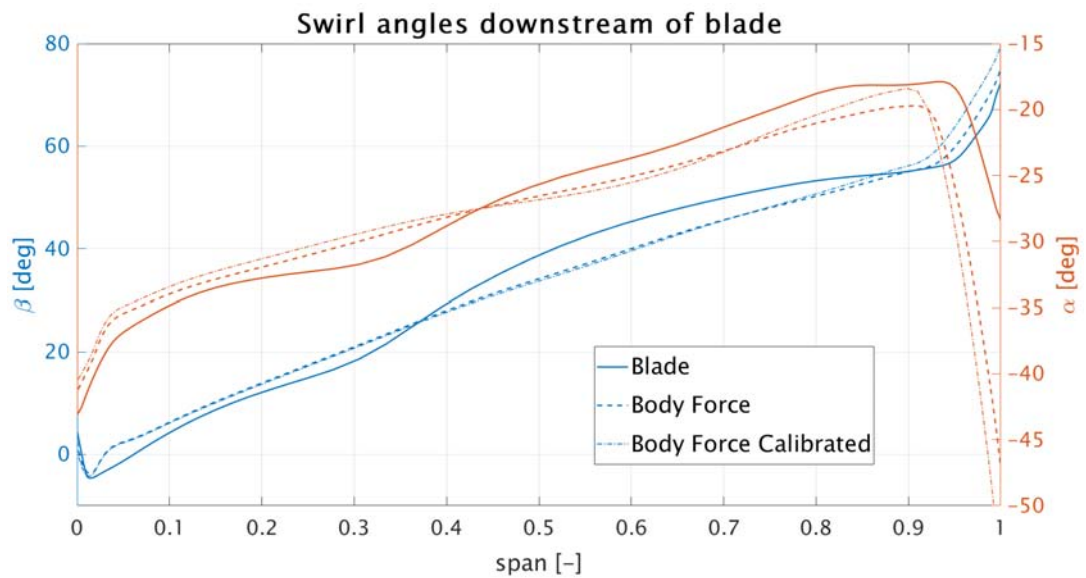


Figure 3.16: Swirl angles ($p_{outlet} = 85000 Pa$)

3.3.8 Pressure and Flow coefficients ($p_{outlet} = 85000 Pa$)

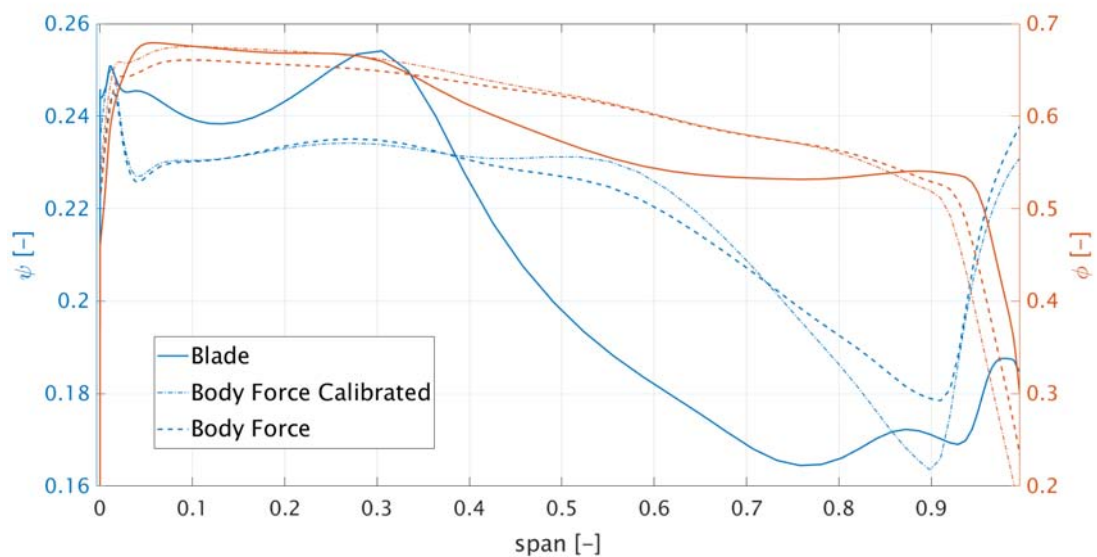


Figure 3.17: Pressure and Flow coefficients ($p_{outlet} = 85000 Pa$)

Chapter 4

Conclusions

The purposes of this thesis were:

1. Implement a specific body force model, the lift/and drag model proposed by Thollet, within a commercial CFD solver (ANSYS Fluent).
2. Use the reproduced model to capture the performance of a subsonic fan stage.

The first goal has been successfully achieved using a custom utility provided by the solver.

As far as the second goal concerns, several simulations have been carried out and single speed line-performance maps have been obtained. The results confirm what reported in reference literature: a well calibrated model allow to re-construct the pitchwise-averaged flow field generated by discrete blades, although mass flow rate and work coefficient are overestimated and peak efficiency is underestimated. However, these limitations are balanced by the key advantages of the body force approach: reductions in computational cost due to simplified mesh topologies and the possibility for steady simulations without rotor-stator interfaces. Furthermore, the same model can be use to simulate different fan geometries: it is sufficient to create and load a new external text file containing the new geometric data.

Especially regarding these last aspects, the model is well suited for use in design to capture fan-airframe interactions. For instance, it can be used in an optimization-loop of a coupled nacelle inlet-fan design: for a fixed inlet geometry, the fan blade shape changes parametrically with each simulation to find the optimal configuration; new geometries can be simulated loading in the model an external text file containing blade geometry informations.

The model can also be used to predict the performance of a fan subjected to several inlet conditions: the onset of flow separation at off-design operating

condition with large angles-of attack is one of the critical considerations in the design of subsonic inlets.

Bibliography

- [1] A. Cavallini, M. Sovrano, and L. Rossetto. *Elementi di gasdinamica*. Progetto Libreria, 2017.
- [2] M. Drela. Making an extraordinary machine better: the d8 aircraft concept. *TEDxNewEngland*, 2012.
- [3] ANSYS Fluent. 14.0 ansys fluent udf manual. *ANSYS, Inc. Canonsburg, PA, USA*, 2013.
- [4] Y. Gong. *A computational model for rotating stall and inlet distortions in multistage compressors*. PhD thesis, Massachusetts Institute of Technology, 1999.
- [5] Y. Gong, C. S. Tan, K. A. Gordon, and E. M. Greitzer. *A Computational Model for Short Wavelength Stall Inception and Development in Multi-Stage Compressors*, volume Volume 1: Turbomachinery of *Turbo Expo: Power for Land, Sea, and Air*. 06 1998.
- [6] D. K. Hall. *Analysis of civil aircraft propulsors with boundary layer ingestion*. PhD thesis, Massachusetts Institute of Technology, 2015.
- [7] E. Hsiao, M. Naimi, J. P. Lewis, K. Dalbey, Y. Gong, and C. Tan. Actuator duct model of turbomachinery components for powered-nacelle navier-stokes calculations. *Journal of Propulsion and Power*, 17(4):919–927, 2001.
- [8] C. Hughes. Aerodynamic performance of scale-model turbofan outlet guide vanes designed for low noise. In *40th AIAA Aerospace Sciences Meeting & Exhibit*, page 374, 2002.
- [9] C. Hughes. The promise and challenges of ultra high bypass ratio engine technology and integration. In *49th AIAA Aerospace Sciences Meeting & Exhibit*, 2011.

- [10] F. Marble. Three dimensional flow in turbomachines, volume x of high speed aerodynamics and jet propulsion. pages 83–166. Princeton University Press, Princeton, 2002.
- [11] A. Peters, Z. S. Spakovszky, W. K. Lord, and B. Rose. Ultrashort nacelles for low fan pressure ratio propulsors. *Journal of Turbomachinery*, 137(2), 2015.
- [12] A. Plas, D. Crichton, M. Sargeant, T. Hynes, E. Greitzer, C. Hall, and V. Madani. Performance of a boundary layer ingesting (bli) propulsion system. In *45th AIAA aerospace sciences meeting and exhibit*, page 450, 2007.
- [13] W. Thollet. *Modélisations simplifiées de turbomachines pour l'analyse par la simulation des installations motrices complexes d'avions*. PhD thesis, Toulouse, ISAE, 2017.